

# Self-centering technique for existing concrete bridge columns using prestressed iron-based shape memory alloy reinforcement

Saim Raza<sup>a</sup>, Robert Widmann<sup>a</sup>, Julien Michels<sup>b</sup>, M. Saiid Saiidi<sup>c</sup>, Masoud Motavalli<sup>a,d</sup>, Moslem Shahverdi<sup>a,d,\*</sup>

<sup>a</sup> Empa, Swiss Federal Laboratories for Materials Science and Technology, Dübendorf 8600, Switzerland

<sup>b</sup> re-fer AG, Seewen 6423, Switzerland

<sup>c</sup> Department of Civil and Environmental Engineering, University of Nevada, Reno, NV 89557, United States

<sup>d</sup> School of Civil Engineering, University of Tehran, Tehran 4563-11155, Iran

## ARTICLE INFO

### Keywords:

Self-centering  
Fe-SMA reinforcement  
Prestressing  
Residual drifts  
Concrete bridge columns

## ABSTRACT

Reinforced concrete (RC) bridge columns are expected to undergo large inelastic displacements during major earthquake events, which in turn can result in residual displacements that can potentially affect the functionality of the bridge. While post-tensioning has been used to develop self-centering column systems for new bridge construction, the self-centering of existing bridge columns remains a challenge, mainly due to the limitations associated with the application of conventional post-tensioning techniques to existing structures. This study aims to address this important research gap by developing a robust self-centering technique to mitigate the residual displacements of the existing bridge columns. The proposed self-centering technique exploits the unique self-prestressing characteristics of iron-based shape memory alloy (Fe-SMA) bars to prestress existing bridge columns. The effectiveness of the proposed technique was evaluated through the large-scale experimental investigation of four columns. The variables of the study included the ratio of steel to Fe-SMA reinforcement, the total longitudinal reinforcement, and the initial prestress. The experimental results showed that the proposed technique could significantly reduce the residual drifts of existing bridge columns. The residual drift of the columns was found to be less than 1% up to a target drift of 4% when the ratio of steel to Fe-SMA reinforcement was  $\leq 0.3$ . The paper concludes with a discussion of the self-centering mechanism of columns reinforced with prestressed Fe-SMA bars, where it is shown that, unlike post-tensioning tendons which do not contribute much to the energy dissipation of columns, prestressed Fe-SMA bars begin to contribute to the energy dissipation after the initial prestressing is lost at high drifts, resulting in an enhanced seismic resilience of the columns.

## 1. Introduction

Vertical load-bearing members such as bridge piers, building columns, and walls experience large inelastic lateral displacements under the lateral forces induced by earthquakes. The lateral load acting on the member returns to zero at the end of the ground motion. However, structural members do not necessarily return to their original position and show permanent displacement known as residual drift. This is particularly true under the fault-normal motions in bridges near earthquake faults [1]. The residual drift can seriously impair the functionality of the bridge because of misalignment of the bridge with the roadway and concerns about bridge safety. For instance, it was reported that approximately 100 reinforced concrete (RC) bridge columns with a

residual drift greater than 1.75% were demolished following Hyogo-ken Nanbu earthquake in 1995 [2], even though the damage in many of the columns was moderate.

Bridges are part of the critical lifeline infrastructure and should remain functional for emergency response after a disaster. To mitigate the problem of residual drifts, research has been carried out over the last two decades to develop self-centering mechanisms for bridge columns to enable them to recover lateral displacements at the end of the earthquake. Self-centering behavior is important because it significantly reduces the repair/demolition work and the associated costs and ensures the functionality of the structure after extreme loading. The conventional approach to adding self-centering characteristics to an RC column is the use of unbonded post-tensioned tendons in the column, which results in a controlled rocking behavior of the column under lateral

\* Corresponding author.

E-mail addresses: [moslem.shahverdi@empa.ch](mailto:moslem.shahverdi@empa.ch), [moslem.shahverdi@ut.ac.ir](mailto:moslem.shahverdi@ut.ac.ir) (M. Shahverdi).

<https://doi.org/10.1016/j.engstruct.2023.116799>

Received 8 May 2023; Received in revised form 18 July 2023; Accepted 21 August 2023

Available online 28 August 2023

0141-0296/© 2023 The Authors. Published by Elsevier Ltd. This is an open access article under the CC BY license (<http://creativecommons.org/licenses/by/4.0/>).

Nomenclature			
$f_y$	yield strength of bar	$\Delta_i$	displacement in each cycle
$f_{cm}$	mean compressive cube strength of concrete	$k_g$	gross stiffness
$f_c$	mean compressive cylinder strength of concrete	$E_{avg}$	average elastic modulus of core concrete and cover shotcrete
$H$	height of the column	$I_g$	gross moment of inertia
$P_G$	gravity load	$I_{eff}$	effective moment of inertia
$P_p$	prestressing load	$L$	shear span length
$A_g$	gross-sectional area	$M_{sc}$	self-centering moment
$\varnothing$	diameter of the bar	$M_{resisting}$	resisting moment
$\rho_l$	longitudinal reinforcement ratio	$D$	diameter of the column
$\rho_{l,t}$	total longitudinal reinforcement ratio	$d_{FC}$	distance from the outermost fiber to the centroid of the concrete compression block
$\rho_{l,steel}$	longitudinal reinforcement ratio of steel	$d_{SMA,i}$	distance from the outermost fiber to the center of the SMA bar
$\rho_{l,sma}$	longitudinal reinforcement ratio of Fe-SMA	$F_{SMA,i}$	force in the SMA bar
$\rho_s$	volumetric ratio of transverse reinforcement relative to the concrete core	$F_{ED,i}$	force in the ED bar
$k_i$	stiffness in each loading cycle	$d_{ED,i}$	distance from the outermost fiber to the center of the ED bar
$F_i$	lateral force in each cycle		

loading [3]. Post-tensioning provides a restoring force to the column to bring it back to its origin upon unloading. Tendons are unbonded to prevent the localization of strains and to allow the tendon to remain elastic even at high drifts. An important drawback to this approach is that unbonded steel tendons are vulnerable to corrosion, thus limiting the field application of this technique [4]. To overcome the problem of corrosion, studies have used Carbon fiber-reinforced polymers (CFRP) tendons for the post-tensioning of bridge columns [4]. Regardless of whether the tendons are made from steel or CFRP, no hysteretic energy dissipation is expected from the tendons because they are designed to remain elastic. To provide energy dissipation capacity, bonded steel bars, also known as energy dissipating (ED) bars, have to be provided at the column-footing joint [5]. It is typically recommended that for self-centering, the contribution of ED bars to total bending moment capacity should be less than 50% [6].

Many previous studies have focused on the development of self-centering systems for precast segmental piers used in accelerated bridge construction (ABC) of new bridges. In some of the studies [7–8], no ED bars were provided in the column, and lateral resistance was solely provided by the post-tensioned tendon, while in others some ED bars were installed to increase the energy dissipation capacity of the columns [9–13]. Other studies have used external replaceable dampers to enhance the energy dissipation of the columns [14–15]. A comparison of the self-centering performance of columns with bonded and unbonded tendons was studied by [16], which showed that bonded tendons experienced large prestress losses and resulted in relatively large residual drifts.

A review of the state-of-the-art shows that while many studies have developed self-centering systems for new construction, the focus on improving the self-centering characteristics of existing bridge columns has been limited [6,17–18]. This is mainly due to the technical difficulties associated with the installation and post-tensioning of tendons in existing columns, as conventional post-tensioning techniques require heavy mechanical equipment, such as hydraulic jacks, anchor heads, etc. Because existing bridge columns are most vulnerable to large permanent displacements, particularly in moderate and high seismic regions, a practical self-centering technique is required to overcome this problem.

Prestressing of existing bridge columns with iron-based shape memory alloy (Fe-SMA) bars can be a promising solution to this problem [19]. Fe-SMA belongs to a class of smart materials that show unique prestressing characteristics upon heating. To generate the prestress/recovery stress in Fe-SMA, the bars are first pretrained to a target value and then unloaded. The pretrained bars are then clamped at both ends

and heated to a target temperature of 160° C or above. Heating the Fe-SMA triggers the shape memory effect, which is the material's ability to recover its inelastic deformations when heated [20–21]. When Fe-SMA is clamped at both ends, the strain recovery is prevented and the shape memory effect results in recovery stress and prestressing of the member. Thus, Fe-SMA can be an attractive alternative to provide self-centering features as it simplifies the prestressing process. Thermal activation of Fe-SMA can be performed either by electrical resistive heating or gas flame heating. A state-of-the-art review of the prestressing applications of Fe-SMA reinforcement for RC structures has been provided by [22]. A number of studies have investigated the use of Fe-SMA bars and strips for the flexural strengthening of RC beams [23–26] and slabs [27–28] and shear strengthening of RC beams [29–31]. The bond behavior of near-surface mounted [32–33] and cast-in-place [34] ribbed Fe-SMA bars has also been investigated in detail. Finite element modelling of Fe-SMA reinforced structures has been carried out in a few studies [35–37]. Fe-SMA plates have also been used as buckling restrained braces (BRBs) [38] but their self-centering potential was limited compared to Ni-Ti SMA BRBs [39–40].

The aim of the study presented in this article was to develop a robust self-centering technique for existing bridge columns by exploiting the unique prestressing characteristics of Fe-SMA bars for earthquake engineering applications. The proposed technique was implemented in four columns and its effectiveness in mitigating the residual displacements of the columns was evaluated through experimental investigation under constant axial loading and quasi-static lateral loading. Details of the experimental programme, including a description of the specimens, the self-centering technique, the experimental set-up, and the loading protocol are provided in the next section. The results of the experimental investigations are then discussed in detail. Finally, the paper concludes with a discussion of the self-centering mechanism of columns prestressed with Fe-SMA bars, its practicality, and benefits/drawbacks.

## 2. Experimental programme

### 2.1. Design of experiments

The most influential factor affecting the residual drift is the amount of bonded ED bars in an RC column. The hysteretic behavior of a conventional column reinforced only with bonded ED bars is shown in Fig. 1 (a). It can be seen that on unloading the column shows a residual drift that keeps on increasing with each loading excursion. The reason for large residual drifts in conventional columns is mainly that steel bars

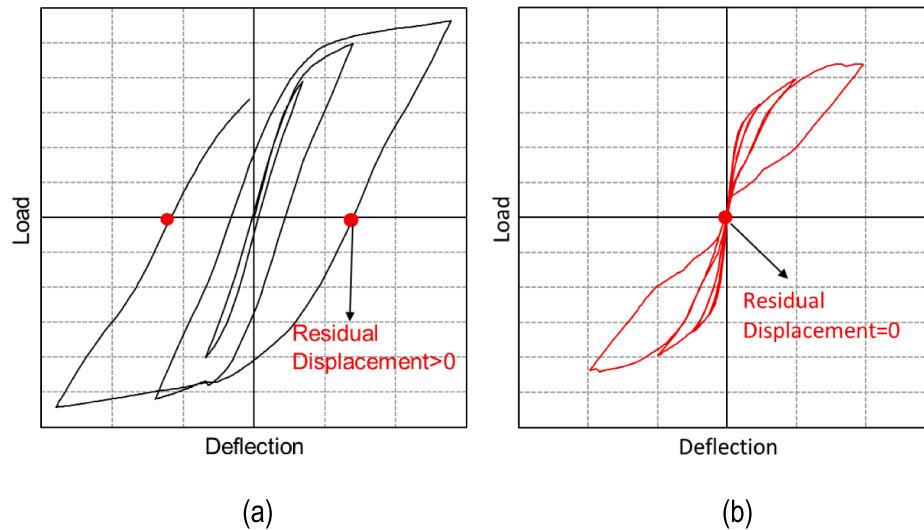


**Fig. 1.** Hysteretic behavior and residual drift of RC columns; a) conventional column with bonded ED bars and no prestressing; b) self-centering column with unbonded prestressed bars.

cannot recover their plastic deformation on unloading, and therefore exhibit large residual strains. It is possible to reduce the residual drift of an RC column by replacing some of the bonded ED bars with unbonded prestressed reinforcement. Fig. 1 (b) shows the hysteretic behavior of a column reinforced with unbonded prestressed bars only, where the column shows no residual drifts on unloading, and the unbonded prestressing bars return the column fully to its original position. This results from the controlled rocking behavior, which involves opening the footing-column joint and provides a mechanism for the column to rock back to its initial position under the action of the prestressing force. However, such columns have significantly lower energy dissipation capacity, as evident from Fig. 1 (b), which is undesirable under earthquake actions. This entails achieving an appropriate balance between the amount of bonded ED and unbonded prestressed reinforcement for adequate energy dissipation as well as effective self-centering.

The design of new columns with appropriate self-centering and energy dissipation characteristics is relatively simple as the amount of bonded ED reinforcement relative to unbonded prestressed reinforcement can be effectively controlled. In contrast, existing bridge columns already have a significant amount of bonded ED bars, therefore, simply providing additional unbonded prestressed reinforcement may not necessarily result in significant self-centering.

The self-centering technique proposed in this study has been developed considering the above-mentioned challenging aspects. To address the challenge relating to the amount of bonded ED bars in existing columns, this study considers the possibility of cutting some of the ED bars to reduce their amount relative to the newly added prestressed Fe-SMA bars. Additionally, to overcome the potential problem of corrosion in the newly added prestressed bars, the idea of partial bonding (instead of full unbonding) is introduced. This is accomplished by using smooth rather than deformed Fe-SMA bars throughout the column height, embedded in a corrosion-resistant shotcrete layer, and with anchorage provided by grouted threaded end region. Yielding in smooth bars spreads thus preventing stress concentration. In this way, the straining and associated loss in the prestress of Fe-SMA bars could also be delayed.

## 2.2. Details of specimens and self-centering technique

The self-centering technique was implemented on four large-scale cantilever column specimens that were designed according to the provisions of EN 1992-2 [41] and EN 1998-2 [42] and represented existing RC bridge columns. The specimens were a 1:4 scale model of the bridge columns. The column diameter and height were 350 mm and 1400 mm,

respectively. The longitudinal reinforcement comprised 6 $\phi$ 14 steel bars corresponding to a longitudinal reinforcement ratio ( $\rho_{l,steel}$ ) of about 1%. The confinement reinforcement was designed following the provisions of EN 1998-2 [42] for a limited ductile behavior and consisted of  $\phi$ 8@80 mm steel ties in the plastic hinge region, resulting in a volumetric ratio of transverse reinforcement relative to the concrete core ( $\rho_s$ ) of 0.93%. The concrete cover of the columns was 40 mm. The size of the column footing and top loading block was 1660  $\times$  1500  $\times$  400 mm and 570  $\times$  750  $\times$  400 mm, respectively. The design details of the original column specimen are shown in Fig. 2. A characteristic compressive strength of 50 MPa was targeted for the concrete mix. The mean compressive strength of the concrete, summarized in Table 1, was determined by experiments on three 150  $\times$  150  $\times$  150 mm cubes on the day of column testing. Grade B500B steel reinforcement with a specified yield strength of  $f_y = 500$  MPa and an ultimate strain at failure ( $\epsilon_u$ ) of 5% was used as longitudinal and transverse reinforcement.

The steps of the proposed self-centering technique are shown in Fig. 3. In the first step, the concrete cover of the original column (shown in Fig. 3 (a)) was removed by hammering, as illustrated in Fig. 3 (b). The next step was the drilling of  $\phi$ 32 holes into the column footing and the top loading block using a diamond core drill, as shown in Fig. 3 (c). The longitudinal Fe-SMA bars were then installed and grouted into the drilled holes, as shown in Fig. 3 (d). Fe-SMA spirals were installed next to restrain the longitudinal Fe-SMA bars against buckling, as shown in Fig. 3 (e). Fe-SMA spirals were used instead of steel because they were available in smaller diameter, i.e. 6 mm, and take up less space. Fig. 3 (f) shows the activation of Fe-SMA bars using a gas torch to generate the initial prestress after the installation and grouting of the longitudinal and transverse Fe-SMA reinforcement. The bars were sequentially heated to a temperature of 200°–220° C during activation. After completion of the activation process and generation of the recovery stress, the Fe-SMA reinforcement was finally embedded in a layer of shotcrete, as shown in Fig. 3 (g).

The removal of the concrete cover in the implementation of the proposed technique was necessary for two reasons: i) to roughen the surface of the old concrete to ensure a strong bond with the new mortar layer and ii) to minimize the change in column size by providing additional space for the installation of Fe-SMA bars. An increase in the column size can inevitably increase the weight and stiffness of the existing bridge column, leading to a larger seismic force demand, which is undesirable.

An alternative to the complete removal of the concrete cover could be surface roughening in conjunction with the installation of Fe-SMA

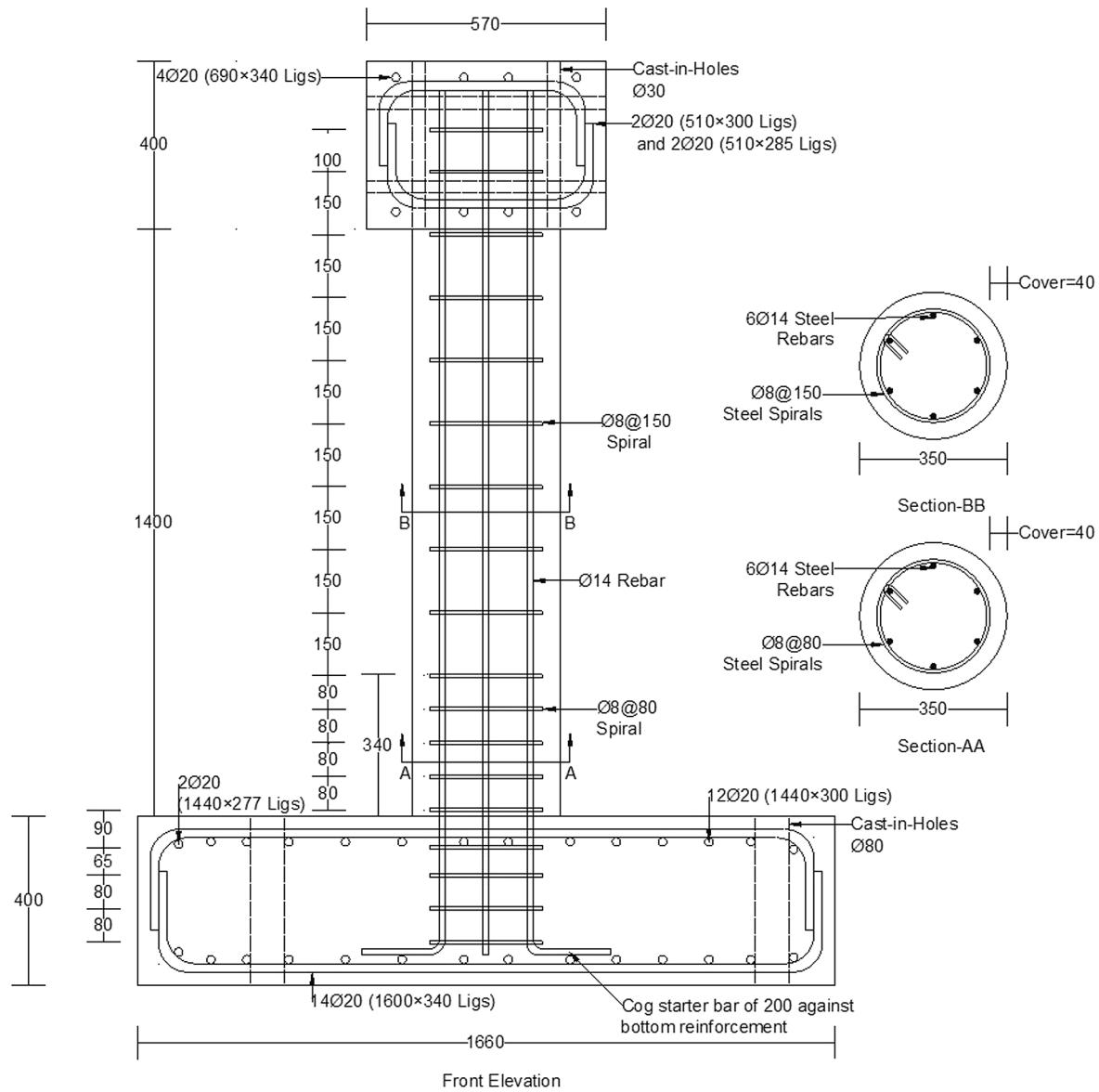


Fig. 2. Design details of original column specimen (All dimensions in mm).

Table 1  
Design details of columns.

No.	D × H (mm)	Compressive Cube Strength ( $f_{cm}$ ) MPa			Longitudinal Reinforcement ( $\rho_l$ , %)		Spirals (mm) ( $\rho_s$ , %)		Axial Load Ratio ( $p/A_g f_c$ )	
		Concrete	Shotcrete	Grout	Steel (uncut)	SMA	Steel	SMA	Prestress $P_p$ (kN)	Gravity Load $P_G$ (kN)
C1	380 × 1400	54	50	90	2 $\phi$ 14 (0.27%)	8 $\phi$ 18 (1.8%)	$\phi$ 8@80 (0.93)	$\phi$ 6@90 (0.37)	591 (0.11)	306 (0.06)
C2	380 × 1400	47	71	91	2 $\phi$ 14 (0.27%)	8 $\phi$ 18 (1.8%)	$\phi$ 8@80 (0.93)	$\phi$ 6@90 (0.37)	595 (0.13)	266 (0.06)
C3	380 × 1400	54	49	90	2 $\phi$ 14 (0.27%)	4 $\phi$ 18 (0.9%)	$\phi$ 8@80 (0.93)	$\phi$ 6@90 (0.37)	288 (0.06)	306 (0.06)
C4	380 × 1400	60	54	90	6 $\phi$ 14 (0.82%)	8 $\phi$ 18 (1.8%)	$\phi$ 8@80 (0.93)	$\phi$ 6@90 (0.37)	643 (0.11)	340 (0.06)

bars in an additional layer of mortar. However, this alternative was not considered in this study because if an additional layer of mortar (with a cover depth of 20 mm to the bars) had been used without removing the concrete cover, the column's diameter would have required an increase of approximately 90 mm (1/4th of the original column diameter), to accommodate the Fe-SMA reinforcement. This would have significantly

altered the stiffness of the column.

Nevertheless, embedding the bars in an additional layer of mortar without fully removing the concrete cover could be an alternative approach for full-size bridge columns with large diameters, where a change of 90 mm in diameter is small relative to the original cross-section size. In such a case, ensuring a strong bond between the old



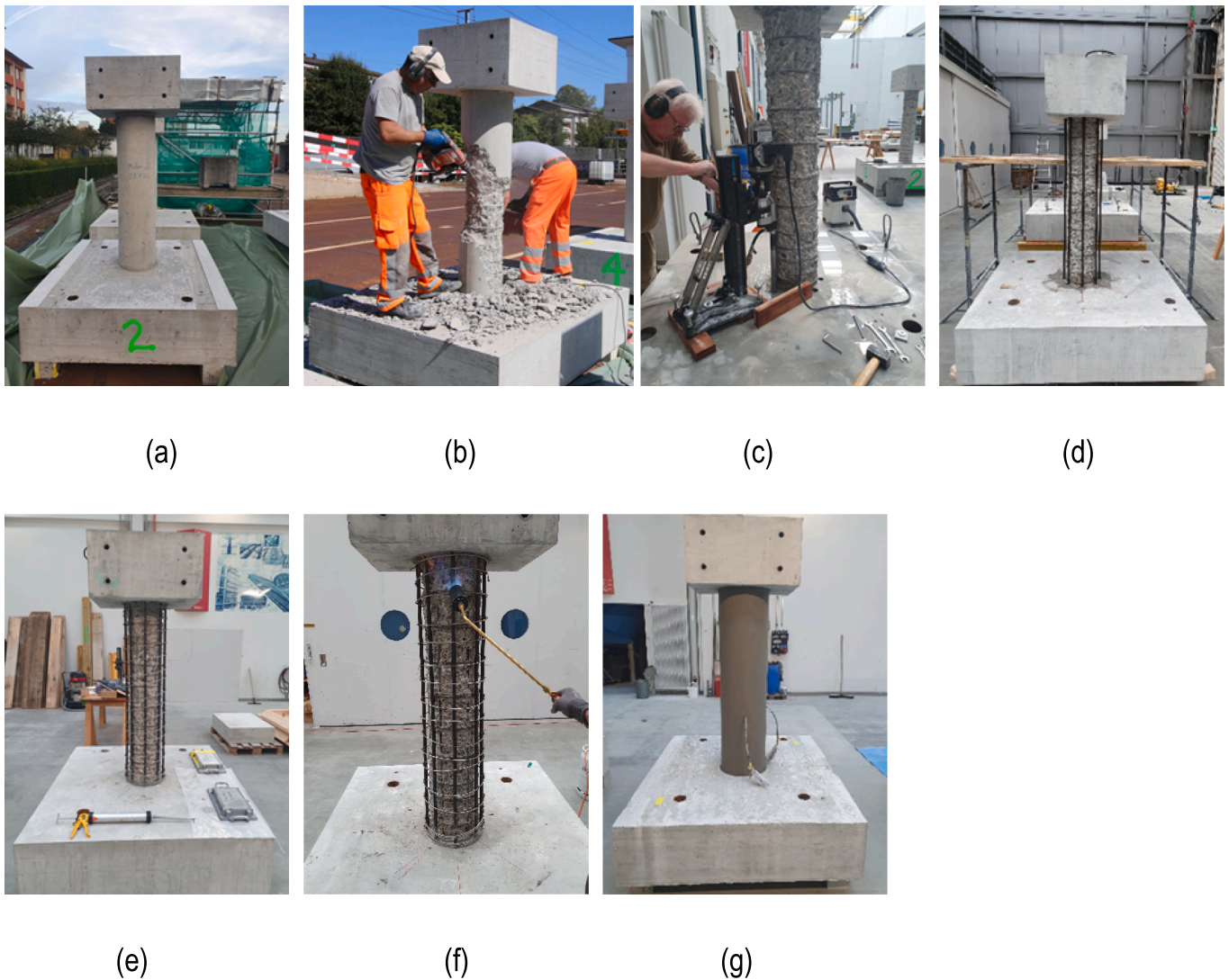


**Fig. 3.** Steps of proposed self-centering technique: a) existing column; b) concrete cover removal by hammering; c) drilling of holes; d) grouted longitudinal Fe-SMA bars; e) installed helical Fe-SMA spirals; f) activation using gas torch; g) after shotcreting.

concrete surface and the new layer remains essential, and this can be achieved through surface roughening of the old concrete.

Table 1 summarises the design details of the columns after cutting some of the original longitudinal steel bars and applying the self-centering technique. The final diameter of the columns was increased to 380 mm to allow for the installation of Fe-SMA reinforcement, as shown in Fig. 4. The variables of this study included the amount of prestressed Fe-SMA bars, the longitudinal steel bars, and the initial prestress. Columns C1, C2, and C4 were provided with 8 $\phi$ 18 longitudinal Fe-SMA bars, while column C3 was reinforced with 4 $\phi$ 18 Fe-SMA bars. Four steel bars of columns C1, C2, and C3 were cut as shown in Fig. 4 (a), (b), and (c), while the steel bars of column C4 were kept intact, as illustrated in Fig. 4 (d). The ratio of bonded steel to partially bonded Fe-SMA bars was 0.15% for columns C1 and C2, 0.3% for C3, and 0.45% for C4. All other parameters were the same for columns C1 and C2, except that shotcrete was applied in two layers on column C2, as shown in Fig. 4 (b). The first layer of shotcrete was applied before the activation of Fe-SMA bars and the second layer was cast after activation. This resulted in prestressing of a larger cross-section in column C2 compared to the rest of the columns. This was done to study the effect of prestressed cross-section depth on the self-centering behavior of the column.

The Fe-SMA bars used in this study were smooth with threaded ends for anchorage into the footing and top loading block. The anchorage

length of post-installed smooth Fe-SMA bars with threaded end anchorage (i.e. similar to the bars considered in this study) was investigated in [43]. The results showed that with an anchorage length of  $14d_b$ , the Fe-SMA bars yielded and developed a stress of about 600 MPa and strain of up to 6% under both monotonic and cyclic loading. Based on these results, a conservative threaded anchorage length of  $20d_b$  was deemed appropriate for the columns considered in this study to allow for the yielding and development of plastic strains in the bar without premature anchorage failure. The smooth portion of Fe-SMA bars extended 50 mm below the footing-column interface to enable a controlled rocking mechanism. A shrinkage-compensated high-strength mortar of type SikagROUT 311 [44], with a maximum aggregate size of 1 mm, was used for bonding the post-installed bars. The holes were made thoroughly wet by injecting water before pouring the mortar to improve the bond. One end of the holes was sealed to ensure that the holes are filled with grout. The grout strength was investigated by testing  $40 \times 40 \times 160$  mm prisms on the day of column testing.

The Fe-SMA bars in C1, C2, and C4 were prestrained to 4% by the manufacturer, whereas those in C3 had an initial prestrain of 10%. This was done to study the effect of higher initial prestrain on the self-centering behavior of columns as it has been reported by [45] that a higher initial prestrain can delay the loss of prestress of Fe-SMA bars. The elastic modulus, yield strength, ultimate strength, and failure strain

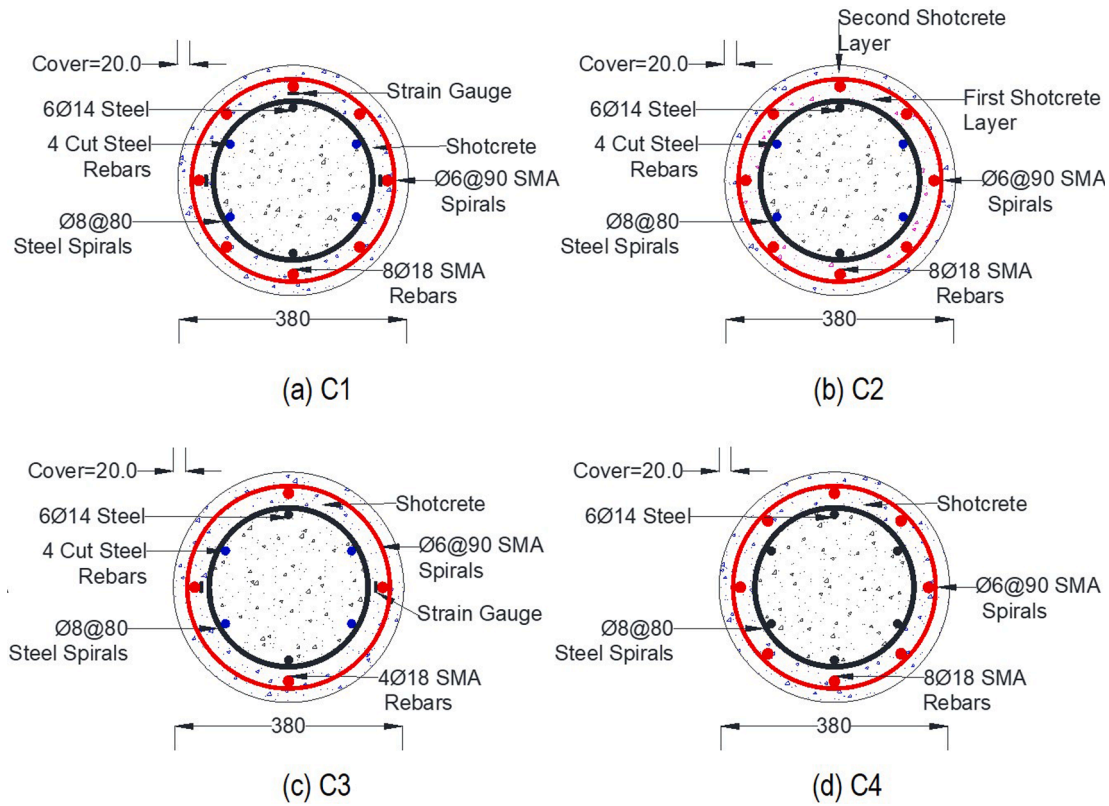


Fig. 4. Design details of column cross-sections after application of the proposed self-centering technique.

of the prestressed Fe-SMA bars used in this study are 75–100 GPa, 400 MPa, 800 MPa, and 40%, respectively. Fig. 5 (a) shows the typical tensile stress–strain behavior of the non-prestrained Fe-SMA bar. The typical stress–temperature behavior of the Fe-SMA bar on thermal activation at different temperatures is shown in Fig. 5 (b). The activation temperature was measured using a digital temperature sensor and was recorded at three locations along the bar. The heating was stopped when the surface temperature of the bar at all three locations was at least 200 °C. The maximum temperature reached in the bar was in the range of 200–220 °C because it is difficult to precisely control the temperature along the bar using a gas torch. The temperature along the Fe-SMA bars

can be controlled more precisely if activation is performed using electric resistive heating rather than gas torch heating. In this case, thermocouples can be mounted at various locations along the length of the embedded bar to monitor the temperature as electric current is passed through the bar ends. An alternative approach could be to ensure that the minimum temperature reached in any section of the bar is at least 250 °C, as the increase in recovery stress of Fe-SMA reaches a plateau between 250 and 300 °C. By targeting this plateau, it is sufficient to use a thermocouple-based sensor to ensure that the minimum temperature in the bar is at least 250 °C when using the gas torch method.

The spirals were made from  $\phi = 6$  mm Fe-SMA wires. The Fe-SMA

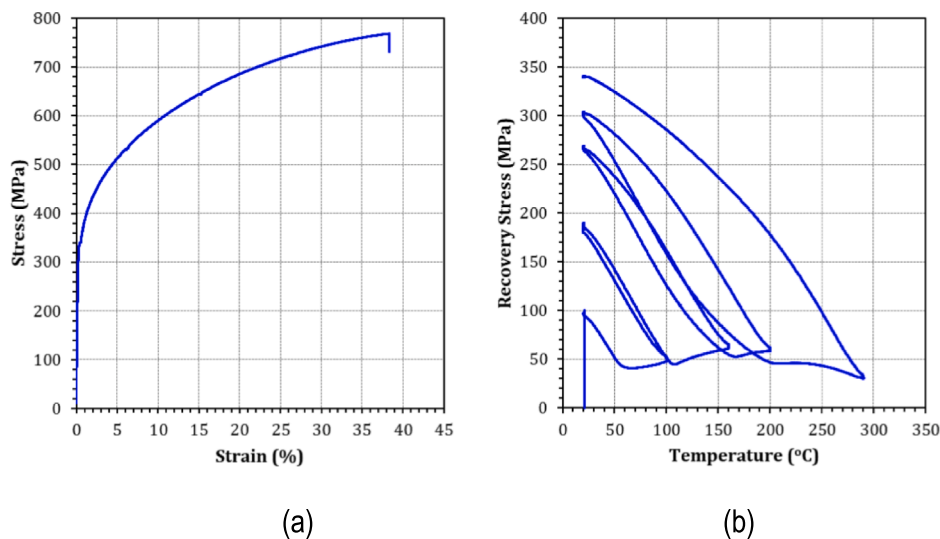


Fig. 5. Behavior of Fe-SMA bars: a) tensile stress vs strain; b) stress vs temperature on thermal activation.



spirals offer the advantage of active confinement, resulting in improved ductility upon activation. However, as the focus of this study was on self-centering, this aspect was not investigated. A 70 mm long, 135° hook was made at both ends of the helical spirals for anchorage into the holes drilled at the top and bottom end of the column using a polyester-based injection mortar ARTFIX KIT 300. The spacing of the spirals was set to be  $5 d_b$  according to the guidelines of Eurocode 8 [42] to restrain longitudinal Fe-SMA bars against outward buckling. The Fe-SMA spirals were non-prestrained, therefore, heating with the gas torch would activate only the longitudinal Fe-SMA bars and spirals would remain non-activated. The elastic modulus, yield strength, ultimate strength, and failure strain of the non-prestrained Fe-SMA spirals used in this study were measured to be 170 GPa, 450 MPa, 880 MPa, and 45%, respectively.

A fiber-reinforced structural repair mortar Sika MonoTop-412 N [46] along with Sika MonoTop-910 N [47] bonding primer was used for shotcreting. The compressive strength of the shotcrete mortar was investigated by testing  $150 \times 150 \times 150$  mm cubes on the day of the column test.

### 2.3. Experimental setup and instrumentation

#### 2.3.1. Setup and instrumentation for activation

Activation takes place by heating the bars using a gas torch to a temperature range of 200–220 °C and regular temperature control. The axial displacements of the columns as a result of the thermal activation of Fe-SMA bars were measured using linear variable displacement transducers (LVDTs) attached to the top loading block, as shown in Fig. 6. The measurements were performed on columns C1, C2, and C3. LVDTs were attached at the four corners of the loading block in columns C1 and C2, as shown in Fig. 6(a). The displacement at the column center line was determined by averaging the displacements of the LVDTs. In C3, two LVDTs attached at a distance of 15 mm on either side of the column center line were used, as shown in Fig. 6(b), and the displacements were averaged to determine the deformation of the column centerline.

#### 2.3.2. Setup and instrumentation for quasi-static cyclic loading

The experimental setup for quasi-static cyclic loading on columns is shown in Fig. 7. A steel reaction frame was installed on the strong floor

of the laboratory. The gravity load was applied to the column loading block using a 2MN actuator and the lateral load was induced using a 630 kN actuator with a stroke capacity of  $\pm 200$  mm. The vertical actuator was bolted to the reaction frame on one end and the head of the loading block on the other end using a pin connection. This arrangement implied tilting of the vertical actuator at large drifts, resulting in the application of an additional horizontal load component to the column. This additional horizontal load component was taken into account during the post-processing of the results. The horizontal actuator was attached to the rigid steel reaction frame on one side and to the column loading block on the other side via a pin connection. The two servo-hydraulic actuators were operated using a digital 2-channel control system, Walter and Bai PCS 8000. The base of the column was fixed to the strong floor of the laboratory with four M60 bolts resulting in a cantilever configuration. The bolts were prestressed to 1MN each.

A total of 13 transducers were used for measurements during the experiments. The locations of the transducers are shown in Fig. 8. The details of the transducers are as follows: T1 and T2 were LVDTs intended to measure the rocking of the column footing. T3 to T6 were LVDTs used to measure the opening at the column-footing joint and to calculate strains in the plastic hinge region. T7 to T10 comprised string potentiometers (SPOTs) to measure the axial displacement of the column. These SPOTs were attached to the four corners of the top loading block. T11 was an LVDT to measure the horizontal slip of the column footing. The recordings in T1, T2, and T11 were near zero indicating no horizontal slip or rocking of the footing. T12 was a laser-based transducer to measure the displacement at the column tip, while T13 was a SPOT used to measure the horizontal displacement of the loading block at the level of the horizontal actuator.

The strain gauges were installed on Fe-SMA bars in columns C1, and C3, as schematically shown in Fig. 4. The strain gauges were attached to the bars at a distance of 50 mm from the footing-column interface. A VIC-3D digital image correlation (DIC) system was also used to record the crack propagation and damage evolution in the plastic hinge region of the columns, as shown in Fig. 8.

### 2.4. Loading protocol

The experiments were performed under the combined actions of

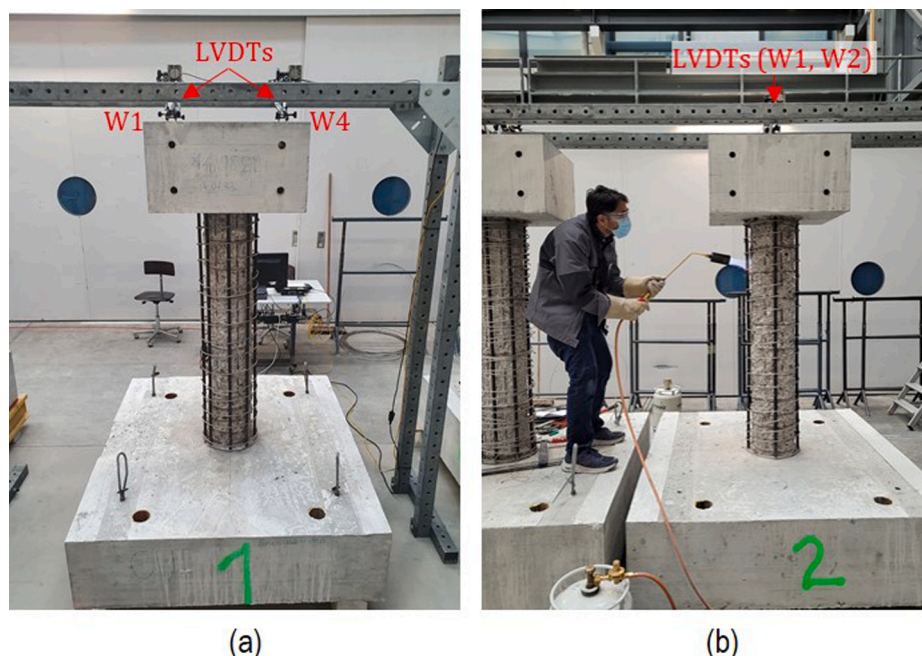


Fig. 6. Measurement setup for recording axial displacements of the column during activation (heating and temperature control): a) C1; b) C3.

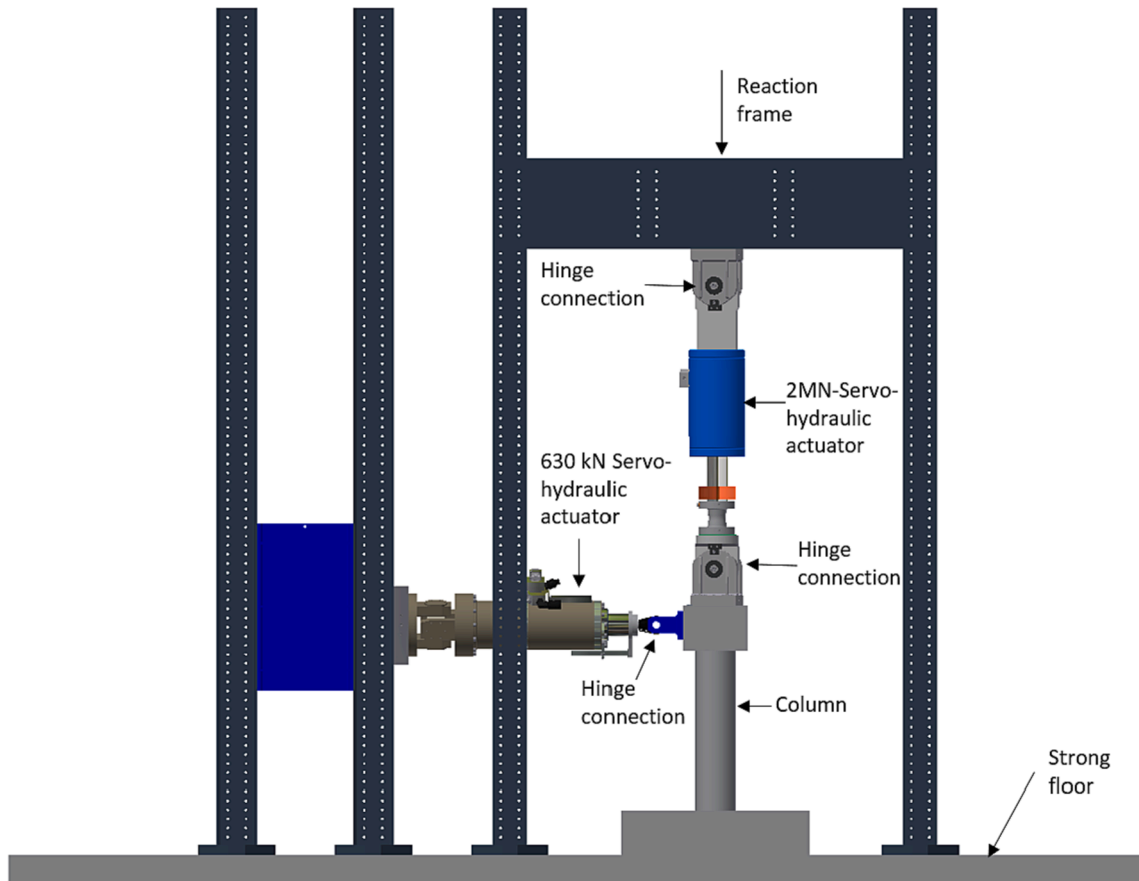


Fig. 7. Schematic details of the experimental setup.

axial compression and cyclic lateral loading. The axial load was applied to the column first and maintained constant throughout the experiment using a load control configuration. The lateral loading comprised quasi-static incrementally increasing cyclic displacements, as shown in Fig. 9. The displacement excursions were repeated twice to capture the strength degradation of the columns under the same displacement amplitude. The following drift amplitudes (in %) were applied to the columns:  $\pm 0.2$ ,  $\pm 0.4$ ,  $\pm 0.6$ ,  $\pm 1$ ,  $\pm 2$ ,  $\pm 3$ ,  $\pm 4$ ,  $\pm 5$  to investigate the full-range elastic/inelastic behavior. The displacements were applied at the column tip and controlled through laser transducer T12. The speed of the displacement-controlled loading was 10 mm/min. The experiment was stopped at a drift of 5% because of the limitations of the experimental setup.

### 3. Results and discussion

#### 3.1. Estimation of initial prestress generated by activation of Fe-SMA bars

The axial deformations of the column during activation were used to estimate the initial prestress generated. Fig. 10 illustrates the evolution of column axial deformations in the first 24 h after activation. It can be noticed that at the beginning of the activation process, the column experienced axial tension. This is because during the early stages of heating at temperatures up to 50 °C, compressive stresses are generated in Fe-SMA due to thermal expansion. In addition, the column elongates due to the thermal expansion of concrete. However, the magnitude of measured displacements during this period (first 1 h after the activation) does not necessarily correspond to axial tensile stress in the column, because as one corner of the loading block moves upwards (refer to LVDT W2 data), the other diagonal corner moves downwards (refer to LVDT W3 data). Once the shape memory effect of Fe-SMA is triggered,

the tensile recovery stresses are produced in Fe-SMA and generate prestressing force in columns.

The average axial displacement of the column after 24 h of activation was used to estimate the axial strains and corresponding axial stress and prestressing load in the column. The measured displacement represented the total axial deformation of the column including the effects of creep. The creep coefficient and corresponding creep strains of concrete were estimated according to the specifications of EN 1992-1-1 [48] and subtracted from the total axial deformation. The age of the columns at the time of loading, (90, 94, and 83 days, respectively, for columns C1, C2, and C3) was taken into account in the creep coefficients. The equations for determining the creep coefficients are not presented here for brevity; the readers are referred to Annex B, B.1 of EN 1992-1-1 [48] for detailed information on the calculation of creep coefficients. Table 2 presents the details of measured axial deformations and corresponding axial stresses generated in the columns.

The comparison of the estimated axial stresses with the theoretical axial stress shows a good correlation, in particular for columns C1 and C2. The theoretical axial stress was computed considering the average cross-sectional diameter of columns as  $C1 = 260$  mm,  $C2 = 285$  mm, and  $C3 = 260$  mm and a nominal recovery stress of 300 MPa in Fe-SMA on thermal activation at 200 °C. The theoretical axial stress takes into account the loss in recovery stress due to the elastic shortening of concrete which was estimated to be 21 MPa per bar for columns C1 and C2 and 11 MPa for C3. The slight difference between theoretical and estimated axial stress for column C3 might be owing to the underestimation of its total axial deformation because of using LVDTs around the centerline instead of the edges. Note that the axial strain was estimated from the measured deformations over a length of 1800 mm (from the top of the loading block to the top of the footing).

The axial load ratio induced by prestressing of Fe-SMA bars was in

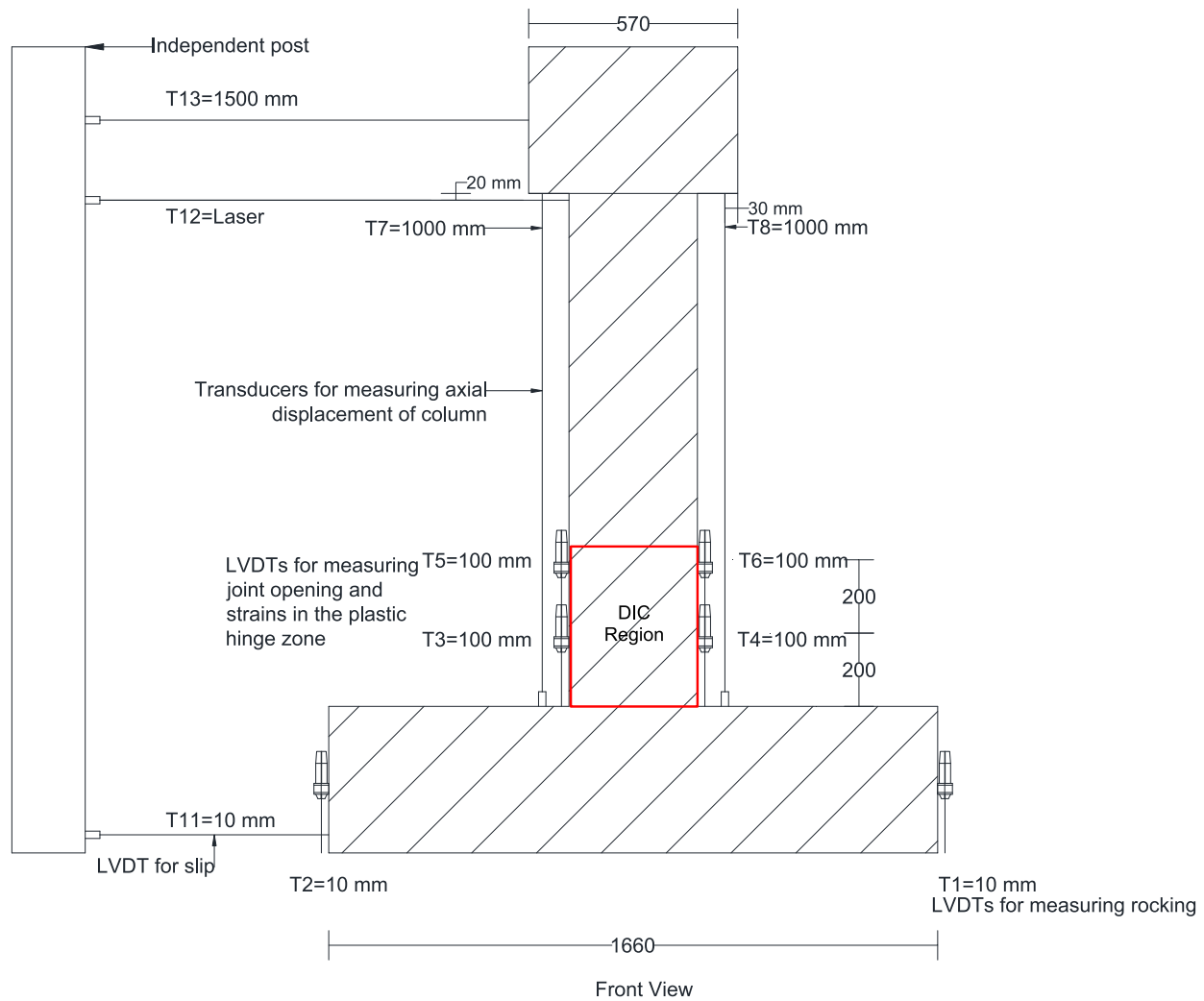


Fig. 8. Details of instrumentation.

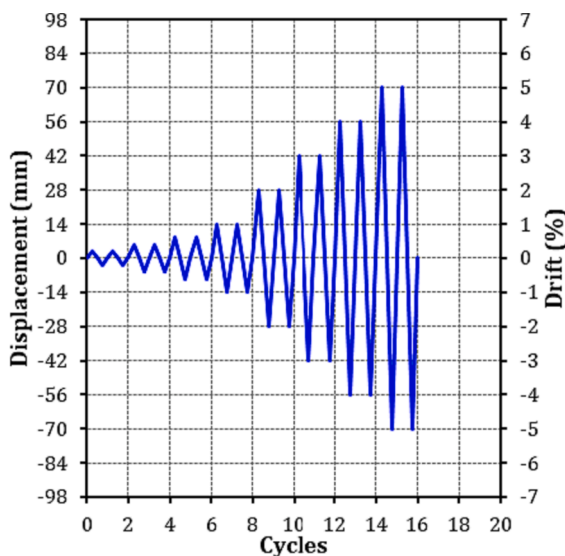


Fig. 9. Quasi-static lateral loading history.

the range of 0.11–0.13 for columns C1, C2, and C4, which is approximately twice the axial load ratio on the columns due to gravity, as summarized in Table 1. In contrast, the axial load ratio due to prestressing and gravity for column C3 was similar and equal to 0.06.

Although the proposed technique is intended for existing columns, the activation of the Fe-SMA bars was conducted without applying gravity axial load due to practical considerations relating to subsequent shotcreting. It would have been challenging to perform shotcreting while the column was axially loaded in the test setup on the strong floor. In practical applications of the proposed technique, prestressing will typically be performed while the column is already under axial load. In such a case, the concrete core will experience higher compressive stresses at the time of prestressing due to the combined effect of prestressing and axial load, and also due to the absence of the shotcrete layer at this point. This in turn could result in higher cracking loads for the concrete core. This is in contrast to the current scenario where the axial load is applied after prestressing and subsequent shotcreting, resulting in relatively less compressive stresses in the concrete core at the time of prestressing.

One consequence of the application of the gravity load after prestressing in this study is that the axial load induced by the Fe-SMA bars was reduced slightly after gravity loading. Measurements from strain gauges attached to the Fe-SMA bars showed that a compressive strain of 0.008% was produced in the bars during the application of the gravity load. This corresponds to a reduction in the recovery stress of approximately 6 MPa in each bar, which is about 2% of the initial recovery stress

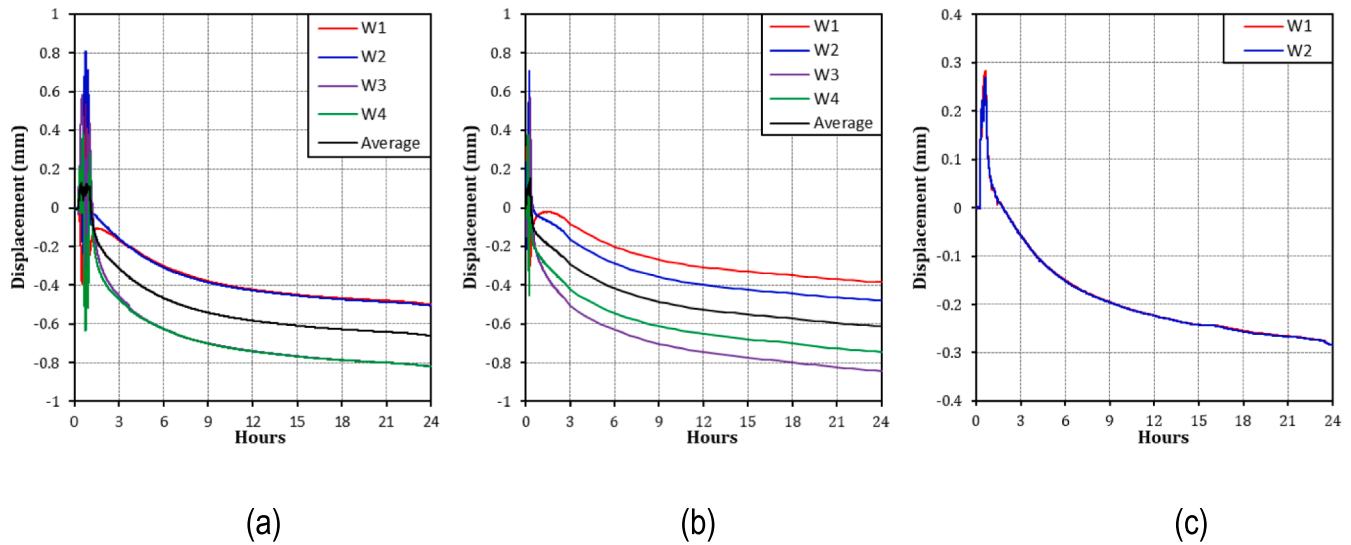


Fig. 10. Axial displacements of the column during activation: a) C1; b) C2; c) C3.

Table 2

Estimated initial prestress in columns after 24 h of activation.

No.	Total Axial Deformation (mm)	Creep Deformation (mm)	Axial Deformation due to prestressing (mm)	Estimated Axial Stress on Concrete (MPa)	Theoretical Axial Stress on Concrete (MPa)
C1	0.66	0.14	0.53	10.1	9.5
C2	0.61	0.15	0.47	8.6	8.0
C3	0.28	0.07	0.21	4.1	4.9

of 300 MPa generated in the bars.

### 3.2. General column response and cracking patterns

All the columns exhibited a controlled-rocking mechanism with a joint opening at the footing-column interface. The joint opening occurred owing to the slippage of smooth Fe-SMA bars at the footing-column joint. The DIC image data was post-processed to investigate the cracking patterns and damage evolution of the columns. In all specimens, the damage initiated in the form of hairline horizontal flexural cracks on the tensile face in the plastic hinge region (i.e. height of 400 mm from the footing-column joint) at drifts  $\leq 0.1\%$ . The flexural cracks grew in width and length with increasing drifts. The tensile splitting cracks emerged under the compressive loading reversal at the 0.8–1.2% drift range, which led to the spalling of the concrete cover at drifts  $\geq 2\%$ . The cover spalling became significant and extensive at 4% and 5% drifts. Reinforcement buckling and fracture were not observed for any specimen, though SMA spirals became visible at the end of the test owing to cover spalling.

The plastic hinge regions of columns C1, C3, and C4 are shown at a drift ratio of +2% (compressive reversal) and -2% (tensile reversal) in Fig. 11 to illustrate the difference between the damage evolution of the columns. Column C2 showed similar behavior to C1, so for brevity, its damage evolution will not be discussed. Fig. 11 shows that cracking and damage of C1, and C3 were more concentrated near the footing-column base joint, whereas the damage of C4 was distributed until the mid-height of the column. This is because of a larger opening at the footing-column base joint in columns C1, and C3 as evident in Fig. 11 (d) and (e), thereby resulting in controlled-rocking behavior and minimizing the damage in the plastic hinge region. The base joint opening was greater in columns C1 and C3 owing to the smaller number of steel bars at the footing-column joint, which in turn resulted in a lesser restraint against the opening of the joint compared to column C4. The vertical splitting cracking was more extensive and significant in column

C4 compared to the other two columns, as shown in Fig. 11. The vertical splitting cracks occur due to bond failure when the local bond of longitudinal reinforcement exceeds the bond stress capacity [49–50]. The higher vertical splitting cracking in C4, therefore, resulted from the larger amount of ED bars in C4, which led to greater bond stresses, compared to the other two columns. The number and width of horizontal flexural cracks were also more extensive in C4 compared to C1 and C3 due to the limited rocking in C4.

The drifts corresponding to various damage states of the column are summarized in Table 3. The results show that among the 4 specimens, C2 had the highest cracking drift, mainly because of the larger prestressed cross-section. Column C3 showed the smallest cracking drift due to lower initial prestress compared to C1, C2, and C4. The cover spalling of column C4 initiated earlier than C1 and C3 due to limited base joint opening. The drifts corresponding to the initiation of vertical splitting crack and spalling of C2 are not known because, after 1% drift, this column was subjected to accidental loading owing to a problem with the controller. The details of this accidental loading are provided in the next section.

The overall damage and displacement profile of the columns at the +5% drift is shown in Fig. 12. It can be observed that all columns exhibited a controlled rocking behavior at the base joint. The figure also illustrates the greater reduction in the cross-section of column C4 at 5% drift owing to cover spalling compared to other columns. The cover spalling extended up to 350 mm from the footing-column joint in column C1, 300 mm in C2 and C3, and 500 mm in C4. These results confirm that introducing low-damage characteristics require a reduction in the number of steel bars at the footing-column interface in addition to the prestressing of the column.

### 3.3. Hysteretic force-displacement behavior

The force-displacement hysteretic behavior of the columns is shown in Fig. 13. It can be noticed that while columns C1, C3, and C4 have a



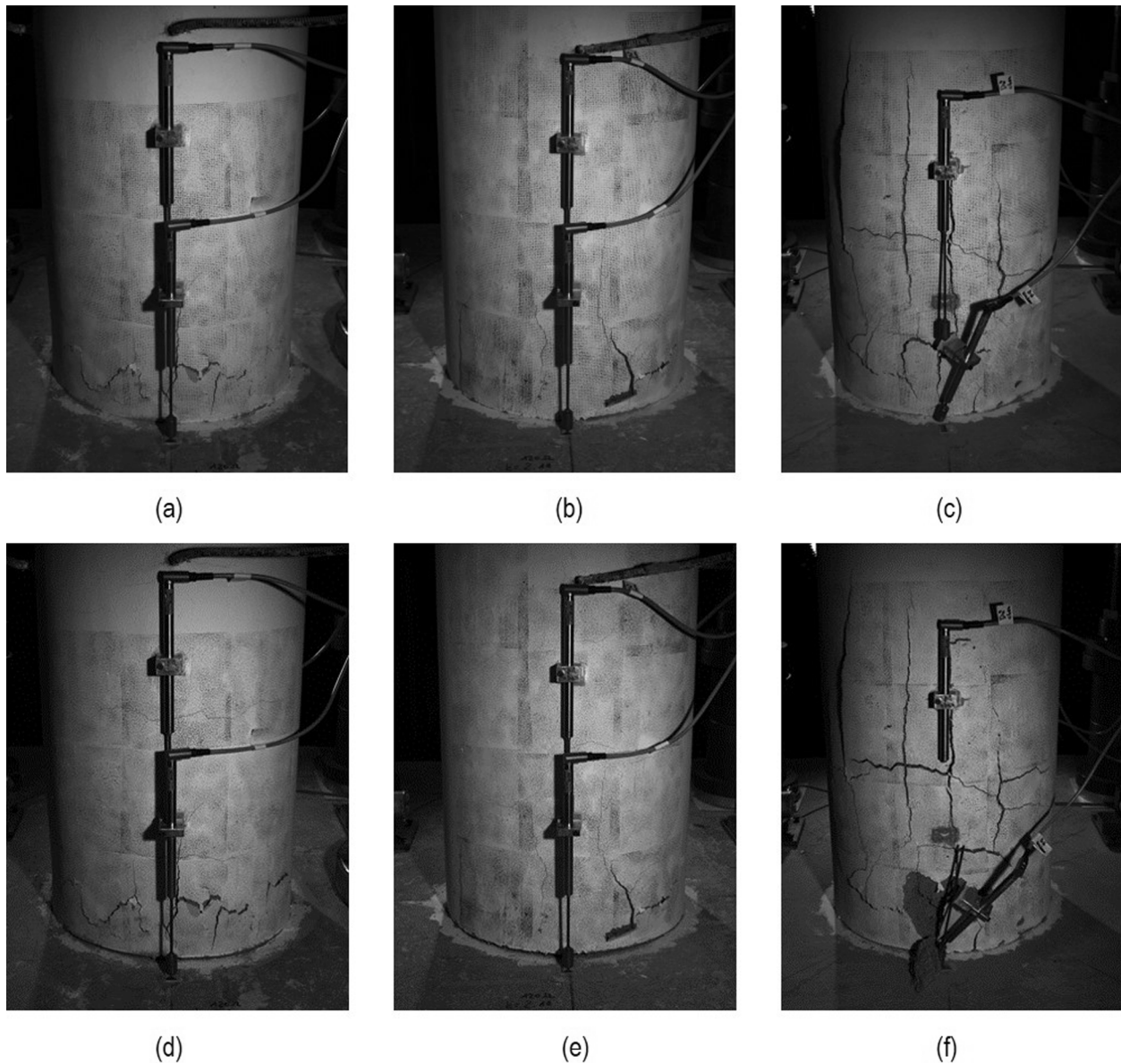


Fig. 11. Cracking patterns of columns; a) C1, b) C3, c) C4 at +2% drift and d) C1, e) C3, f) C4 at -2% drift.

Table 3

Drifts corresponding to various damage limit states of the columns.

No.	Drift (%) at the initiation of		
	Flexural cracks	Vertical splitting cracks	Cover spalling
C1	0.07	0.8	2.5
C2	0.13	n.a	n.a
C3	0.03	1	2.5
C4	0.1	1.2	2.0

regular and symmetrical hysteresis, column C2 has an irregular hysteresis, which is due to the accidental loading it was subjected to during the experiment. The accidental loading occurred due to a problem with the controller after the 1% drift cycle. Due to the problem, the actuators lost control and the column was accidentally subjected to drifts of  $-2.5\%$ ,  $+3.2\%$ ,  $-2.94\%$ , and  $+4.2\%$  directly after the planned cycle of 1% drift at a very fast speed in just 5 s. Within this time, the system was stopped using emergency controls to prevent any further loading. Following the accidental loading, the column was subjected to the remaining planned drift cycles. However, as the column was already damaged, the loading

cycles were not repeated twice and the maximum drift at which the experiment stopped was also reduced to 4.5% instead of 5%.

The effect of three variables considered in this study i.e. longitudinal reinforcement ratio, the ratio of the steel to prestressed Fe-SMA bars and the amount of initial prestress on the hysteretic behavior of the columns is described in the next sub-sections.

### 3.3.1. Effect of longitudinal reinforcement ratio ( $\rho_{lt}$ )

The total longitudinal reinforcement ratio ( $\rho_t$ ), including steel and Fe-SMA bars was 2.1% in columns C1, C2, 1.2% in C3, and 2.6% in C4. The highest load capacity was demonstrated by column C4 with the largest  $\rho_t$  and the lowest load capacity was for C3 with the smallest  $\rho_t$ . The higher damage to concrete in column C4 could be attributed to the fact that this column resisted higher loads compared to the other columns. The maximum lateral load capacity exhibited by the columns and the corresponding drift level is summarized in Table 4. Columns C1, C2, and C4 reached the ultimate load capacity at drifts  $\geq 2\%$ , whereas column C3 achieved the ultimate load capacity at about 1% drift. This is because of the lower amount of total longitudinal reinforcement ratio in C3. The strength degradation was also more severe in C3 compared to

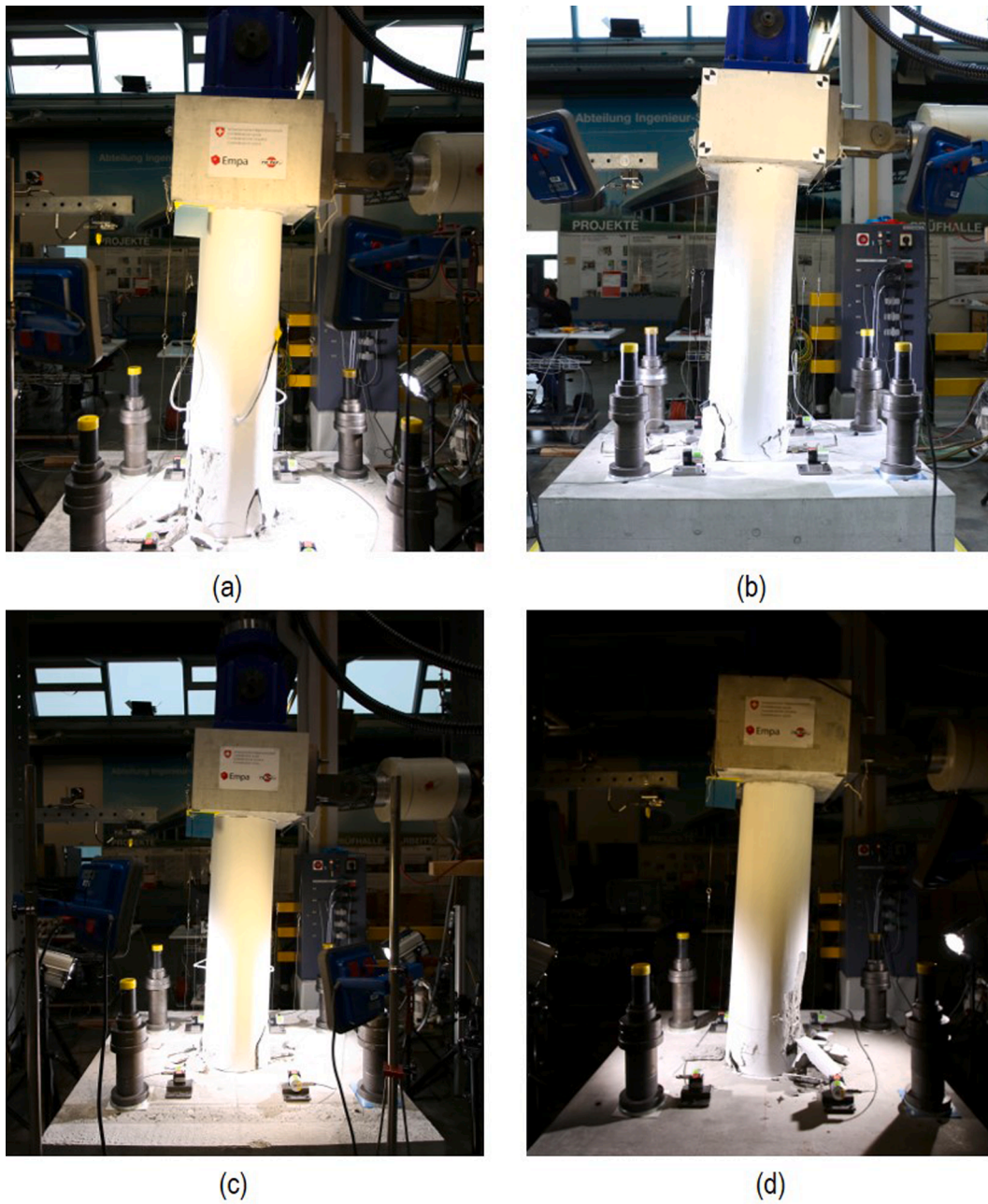


Fig. 12. Damage and displacement profile of the columns at +5% drift: a) C1; b) C2; c) C3; d) C4.

the other columns. Column C3 experienced about 25% degradation in ultimate lateral strength at 5% drift, which is quite high compared to columns C1 and C4, which showed strength degradation in the range of 10–13%. The strength degradation pattern in C2 cannot be compared with that of the other columns due to accidental loading.

### 3.3.2. Effect of the amount of steel to Fe-SMA reinforcement ( $\frac{\rho_{steel}}{\rho_{sma}}$ )

The ratio of the amount of steel to Fe-SMA reinforcement ( $\frac{\rho_{steel}}{\rho_{sma}}$ ) was 0.15 for columns C1, C2, 0.3 for C3, and 0.45 for C4. Fig. 13 shows that columns C1 and C2 with the smallest  $\frac{\rho_{steel}}{\rho_{sma}}$  had the lowest residual drift on unloading at high drifts. In contrast, column C4 with the highest  $\frac{\rho_{steel}}{\rho_{sma}}$  showed the largest residual drift on unloading. Meanwhile, column C3 showed an intermediate behavior. Besides improvement in residual drifts, the degradation in the ultimate lateral strength of C1 was 10% at 5% drift compared to 13% degradation in C4. This could be attributed to

the smaller amount of steel reinforcement in C1 compared to C4, which allowed relatively higher rocking at the base joint leading to lesser damage to concrete and degradation in lateral strength. Column C4 exhibited a wider hysteresis, which is indicative of higher energy dissipation compared to the other columns.

### 3.3.3. Effect of initial prestress

The initial prestressing force in column C3 was one-half of that in the rest of the columns. As a result, C3 showed lower initial stiffness compared to the other columns. Additionally, it can be noticed from the hysteresis that C3 exhibited higher average residual drifts at large drift levels compared to C1 and C2 because of the lower prestressing. The cracking loads, energy dissipation capacity, and ultimate lateral load capacity of C3 are also lower than those of the other columns.



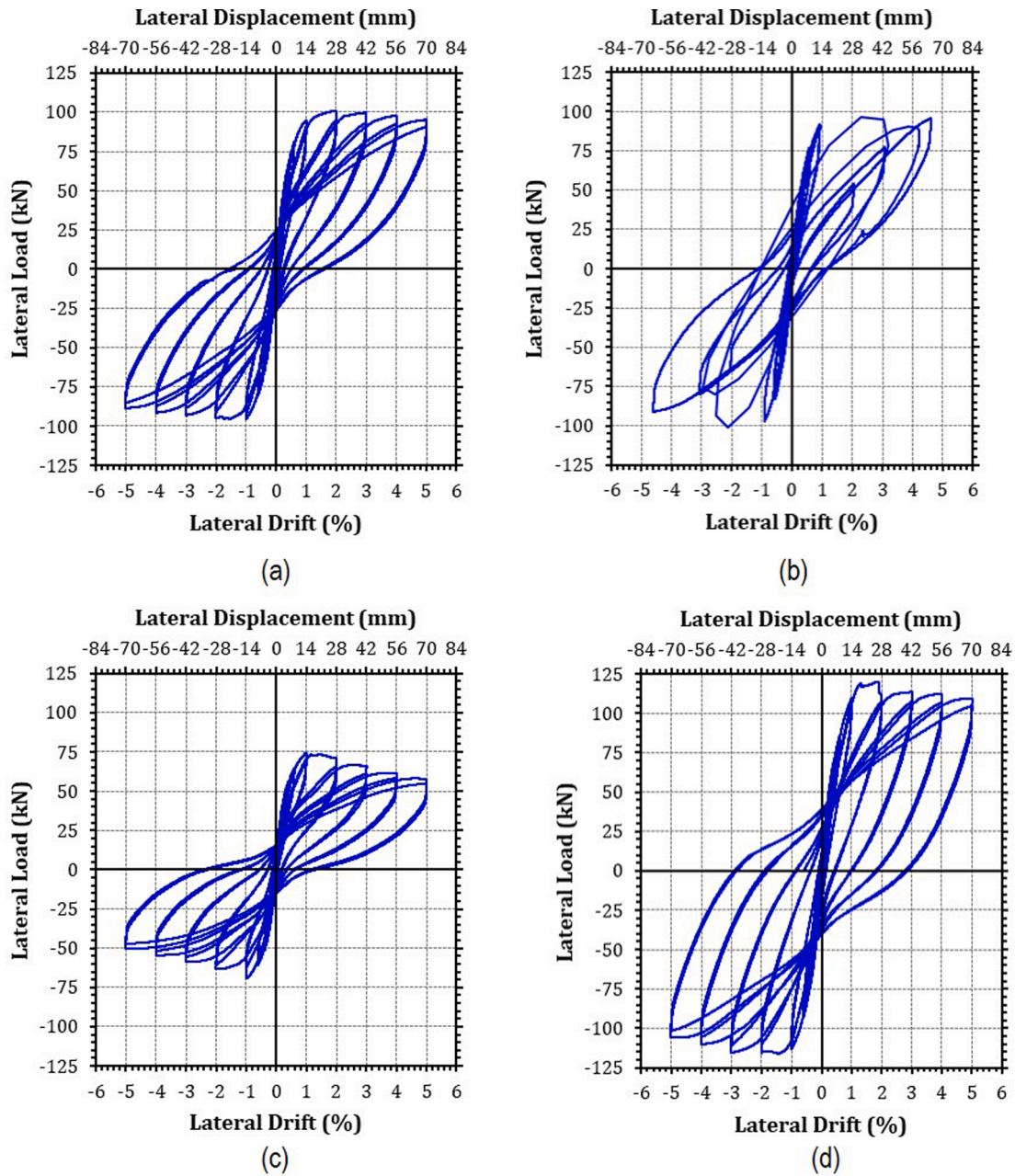


Fig. 13. Hysteretic force-displacement behavior of the columns: a) C1; b) C2; c) C3; d) C4.

Table 4

Ultimate lateral load capacity of the columns.

No.	Ultimate Lateral Load Capacity (kN)		Drift (%)	
	Push	Pull	Push	Pull
C1	+101	-95	+2	-2
C2	+97	-101	+2.3	-2.1
C3	+74	-69	+1	-1
C4	+120	-116	+1.9	-2

### 3.4. Fe-SMA bar strains

The strains in the outermost Fe-SMA bars in the loading direction were measured in columns C1 and C3. The strain gauges were attached to three Fe-SMA bars in C1, as shown in Fig. 4(a). Two of the strain gauges were attached to the outermost bars while one strain gauge was

mounted on the bar located at the neutral axis. Two strain gauges were also attached to the outermost Fe-SMA bars in C3, as shown in Fig. 4 (c). The maximum tension-compression strains in the outermost bars in column C1 were in the range of 0.8–0.9%, whereas the bar located at the neutral axis region experienced a maximum tensile strain of 0.38%, and negligible compressive strains, as shown in Fig. 14 (a). Likewise, the outermost bars in C3 experienced maximum tension-compression strains in the range of 0.8–1.1%, as shown in Fig. 14 (b). The amplitude of the bar strains can provide information about the drift corresponding to the loss of recovery stress in the Fe-SMA. Previous studies [45] have shown that Fe-SMA bars prestrained to 4% can completely lose initial recovery stress at cyclic strain amplitudes of about 0.4%. This implies that the outermost bars lost initial recovery stress at about 2% drift level. In contrast, the bar at the neutral axis lost most of its recovery stress at about 5% drift. This means that up to a drift of 4%, column C1 may have retained some of the initial prestress. The bars in column C3 were prestrained to 10% to increase the strain amplitude associated with

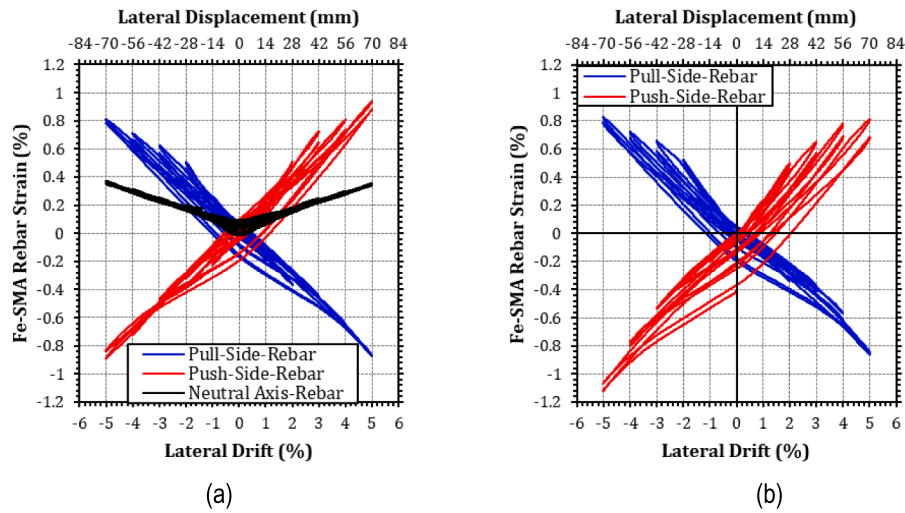


Fig. 14. Fe-SMA bar strains vs lateral drift of the columns: a) C1; b) C3.

complete loss of recovery stress to about 0.8% based on the findings of [45]. The results in Fig. 14 (b) for C3 show that the outermost bars developed a strain of 0.8% at about 4% drift level. It could be inferred from this that these bars completely lost initial recovery stress when the column was pushed to a drift of 4%. However, to get more precise and conclusive information about the column drifts corresponding to the loss in recovery stress, a load cell should be used in future studies.

Fe-SMA bars in C1 experienced more or less symmetric strains in tension and compression. However, in C3, while the pull-direction bar experienced similar strains in tension and compression, the bar in the push-loading direction experienced relatively higher strains in compression. This could be because the column might have developed some inclination/tilt towards the push side after prestressing. As a result, the push-loading direction bar showed a significantly higher residual strain when the column was brought back to its origin after each drift excursion. Consequently, column C2 exhibited higher residual drift in the push direction compared to the pull direction.

### 3.5. Residual drifts and self-centering

The residual drifts exhibited by each column on unloading from the push-pull cycles were calculated from the force-displacement hysteresis for the 2nd load cycle at target drifts of  $\pm 1\%$ ,  $\pm 2\%$ ,  $\pm 3\%$ ,  $\pm 4\%$ , and  $\pm 5\%$ . For a better evaluation of the self-centering performance, the residual drifts of the columns are compared with conventional non-prestressed RC columns from two previous studies [51–52]. The conventional column in Raza et al. 2020 [51] had a total axial load ratio of 0.15, similar to columns C1, C2, and C4 of the current study, while the column in Liu et al. 2020 [52] had a relatively lower axial load ratio of 0.07. The ED steel reinforcement ratio was 1.6% and 1.5%, in the columns of Raza et al. [51] and Liu et al. [52], respectively. The residual drift limit corresponding to a compromise in the functionality of the bridge, thereby warranting its replacement has been chosen as 1% following the recommendations in the literature [53–54]. Fig. 15 shows that columns C1 and C2 were able to maintain a residual drift of  $\leq 1\%$  in

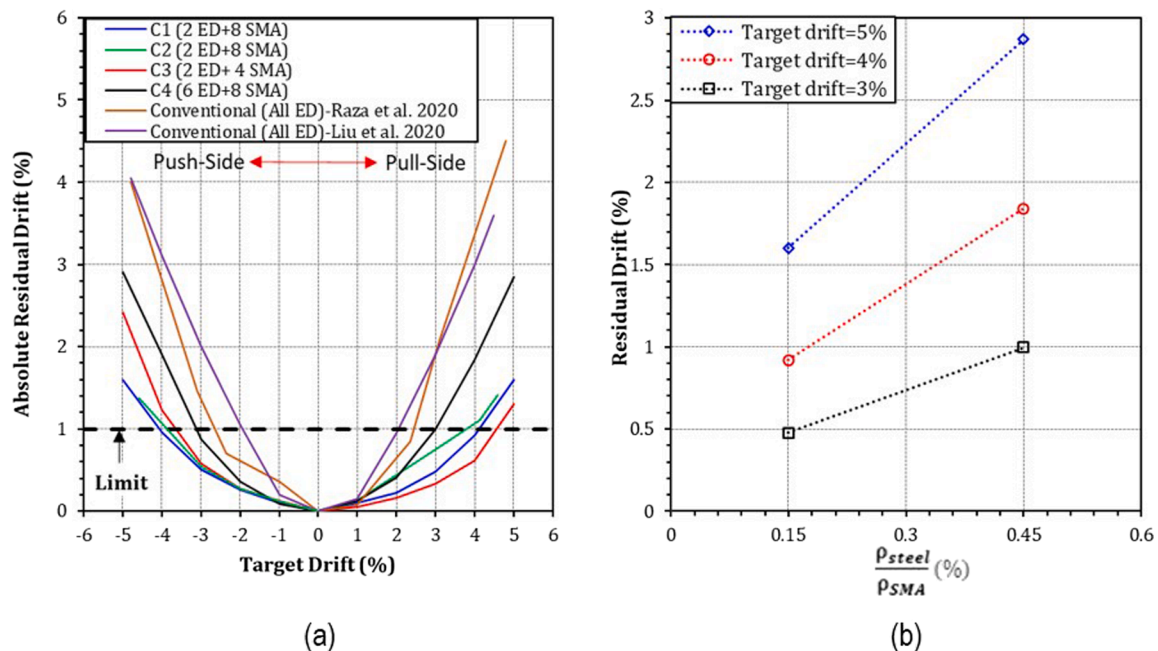


Fig. 15. Residual drifts and self-centering of columns: a) comparison of residual drift of Fe-SMA prestressed columns with conventional non-prestressed RC columns; b) effect of steel to Fe-SMA reinforcement ratio on the residual drift.

the push and pull loading directions until a target drift of 4%. This is because these columns retained some part of the initial prestress until 4% drift, as discussed previously. Fe-SMA bars are expected to behave similarly to ED bars after the complete loss of the initial recovery stress by contributing to the energy dissipation capacity of the columns and increasing the residual drifts. Therefore, the residual drift of column C1 increased by 60% from 1% to 1.6% as the amplitude of the target drift increased from 4% to 5%. Column C3 also exhibited smaller residual drifts in general, however, its residual drift behavior was quite asymmetric in the push-pull directions. The residual drift of C3 was about 2.5% in the push direction as opposed to a residual drift of about 1.3% in the pull direction at a target drift of 5%. This asymmetry in the residual drifts can be attributed to larger compressive strains and corresponding residual strains experienced by the Fe-SMA bar on the push face of the column. The Fe-SMA bar strain vs lateral drift plot of column C3 shown in Fig. 14 (b) illustrates that the maximum strains developed in the pull and push direction bars were  $-0.9\%$  and  $+0.8\%$  when the column was pulled to  $+5\%$  drift, whereas the maximum bar strains were  $+0.8\%$  and  $-1.1\%$  when the column was pushed in the opposite direction. Additionally, on unloading from  $-5\%$  drift to the origin, the residual strain in the push-side bar was about  $-0.4\%$  which is almost double the residual strain in the bar on unloading from  $+5\%$  drift. The higher residual strains led to larger residual lateral forces and corresponding residual drifts in the push-loading direction.

Column C4 showed residual drifts of  $\leq 1\%$  up to the target drifts of 3%. Thereafter, the residual drifts increased, reaching an amplitude of about 2.8% at a target drift of 5%. The relatively higher residual drifts in C4 compared to the other three columns are owing to the higher amount of ED bars in this column. All four columns considered in this study showed significantly better self-centering behavior than the conventional RC columns. Fig. 15 shows that the residual drifts of columns C1 and C2 were about 60% smaller than the conventional columns at 5% target drift. Similarly, the residual drifts of columns C3 and C4 were on average smaller than the conventional columns by 50% and 30%, respectively.

The experimental results show that the ratio of the amount of steel to prestressed Fe-SMA reinforcement ( $\frac{P_{l,steel}}{P_{l,sma}}$ ) affects the self-centering performance most significantly. The effect of  $\frac{P_{l,steel}}{P_{l,sma}}$  ratio on the residual drift of the columns at target drifts of 3%, 4%, and 5% is shown in Fig. 15 (b). The comparison is shown for columns C1 and C4 which had a similar amount of Fe-SMA but different steel reinforcement. The results show that, with all other parameters kept constant, increasing the  $\frac{P_{l,steel}}{P_{l,sma}}$  ratio from 0.15 to 0.45 approximately doubles the residual drift of the column at target drifts of 3%, 4%, and 5%.

### 3.6. Base joint opening

The DIC measurements were used to determine the extent of the opening at the footing-column base joint at different drift levels. Fig. 16 shows the results of the base joint opening for columns C1, C3, and C4. The base joint opening data was not available for column C2 due to accidental loading. The DIC measurements for column C4 were also available for up to 2% drift only, so its base joint opening was calculated up to 2% drift.

The opening at the footing-column joint initiated at a drift of 0.4% for all columns owing to the slippage of smooth Fe-SMA bars at the interface as a result of bond strength deterioration. The results indicate a similar base-joint opening trend for columns C1 and C3. This is probably because of the same amount of ED bars in both columns which provided restraint against the opening, though the amount of Fe-SMA bars was different. The base joint opening of column C4 was significantly smaller than that of columns C1, and C3, mainly because of an increased restraint due to the provision of 3 times more ED bars. Consequently, at 2% drift, the base joint opening of column C4 is approximately 50% of

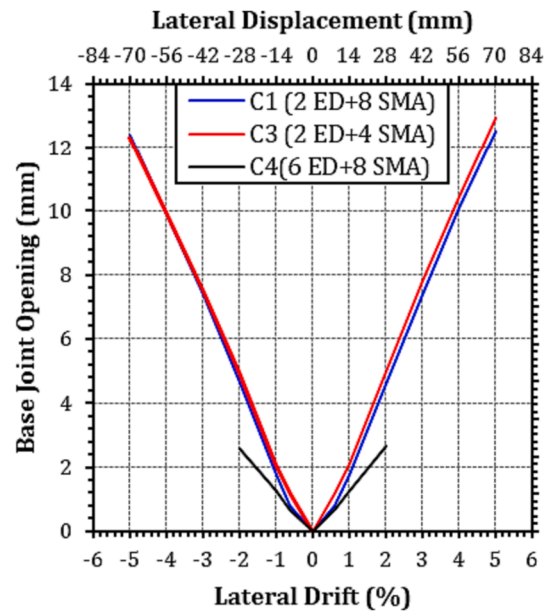


Fig. 16. Base joint opening at the footing-column interface.

the corresponding base joint opening of columns C1 and C3.

The maximum opening of the base joint in columns C1 and C3 was found to be in the range of 12–13 mm at 5% drift. This large opening at the base joint shows that the strain penetration of the smooth Fe-SMA bars resulted in the fixed-end rotation of the column, particularly due to the 50 mm long smooth section of the Fe-SMA bar anchored into the footing. As a result, the total deformation of the columns consisted of a significant portion of displacement due to the fixed-end rotation in addition to flexural and shear deformations, particularly at large drifts. It is worth noting that, for a given load level, such columns experience a greater total displacement and therefore exhibit a lower stiffness than conventional columns with flexure-dominated behavior. It is important to include this fixed-end rotation in the numerical and analytical modelling of the hysteretic behavior of the tested columns. Ignoring the fixed-end rotation will result in an underestimation of the column deflection at a given load and an overestimation of the lateral stiffness.

### 3.7. Energy dissipation

The energy dissipation capacity of all columns was determined by calculating the area enclosed by the force-displacement hysteresis in each loading cycle. The total hysteretic energy dissipation of the columns is shown in Fig. 17 (a). The results indicate that the highest energy dissipation was for column C4 which had the largest amount of ED bars. Column C1 showed an intermediate energy dissipation capacity that was about 32% less than C4. Columns C2 and C3 demonstrated the lowest energy dissipation capacity which was about 50–60% less than C4. The low energy dissipation capacity of column C2 despite a similar design to C1 is because C2 was subjected to only 1 cycle of drifts after the accidental loading. As a result, the total displacement excursion of column C2 during the experiment was about 33% less than the excursion of column C1. Accordingly, the energy dissipation capacity of C2 was about 39% less than C1. The comparison of the total energy dissipation and residual drifts of columns C1 and C3 shows that C1 outperformed C3 in terms of exhibiting smaller residual drifts, as well as greater energy dissipation. Note that for optimal seismic performance, it is important to maintain a balance between the energy dissipation capacity and residual drifts, as they are inversely related. While smaller residual drifts are essential to ensure the post-earthquake functionality of bridges, it is also important to have adequate energy dissipation capacity. This is because lower energy dissipation during seismic actions can increase the seismic



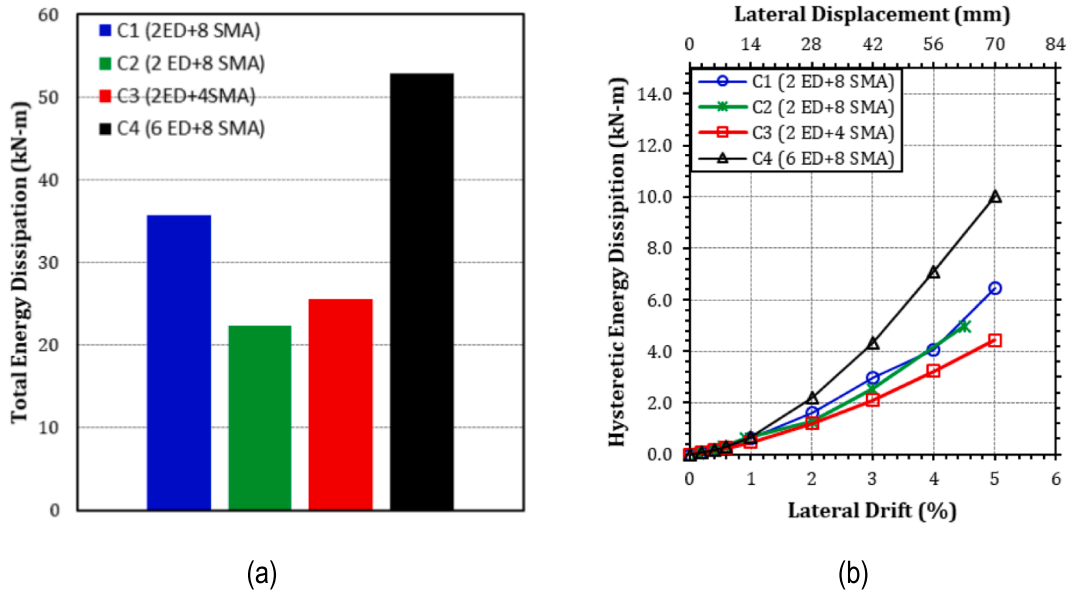


Fig. 17. Energy dissipation behavior of columns; a) total energy dissipation; b) evolution of energy dissipation with increasing drifts.

displacement demand on the columns. Such columns may experience larger displacements to dissipate the seismic energy demand imposed by the earthquakes.

The evolution of the energy dissipation of the columns with each load cycle is shown in Fig. 17 (b). It can be seen that all columns dissipated similar energy up to 1% drift. The energy dissipation capacity of the columns started to evolve differently after 1% drift, with column C4 showing the greatest increase in energy dissipation with each load cycle owing to the largest amount of ED bars and total longitudinal reinforcement ratio. Columns C1 and C2 showed similar evolution of energy dissipation capacity with each load cycle. Column C3 showed the smallest increase in energy dissipation capacity with each load cycle owing to the smallest amount of longitudinal reinforcement. A comparison of the energy dissipation at 5% drift shows that the energy dissipation capacity of column C4 was approximately 35% higher than C1 and 55% higher than C3. This trend in the energy dissipated in the 5% drift load cycle correlates well with the difference in the total energy dissipation of these columns.

### 3.8. Stiffness degradation

The stiffness of the columns was determined using Eq. (1) by averaging the forces and displacements in each loading cycle. The measured stiffness was normalized with the theoretical gross stiffness ( $k_g$ ) of the column given by Eq. (2). The moduli of elasticity of both concrete and shotcrete were taken into account to determine the theoretical gross stiffness of the columns. The average modulus of elasticity ( $E_{avg}$ ) was estimated considering the relative contributions of the core concrete and outer shotcrete layer. For reference, the modulus of elasticity of shotcrete was about 20 GPa [46], and that of the core concrete was in the range of 32.5 GPa to 36 GPa depending on the concrete compressive strength. The shear span length ( $L$ ) of the column was 1400 mm.

$$k_i = \frac{|+F_i| + |-F_i|}{|+\Delta_i| + |-\Delta_i|} \quad (1)$$

$$k_g = \frac{3E_{avg}I_g}{L^3} \quad (2)$$

The progression of the stiffness degradation of the columns with increasing drifts is shown in Fig. 18. The highest initial stiffness was exhibited by column C4 owing to the largest amount of longitudinal

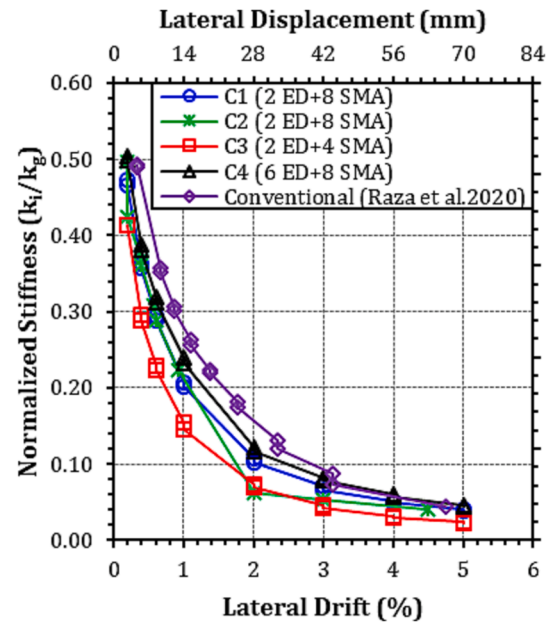


Fig. 18. Stiffness degradation of the columns with increasing lateral drifts.

reinforcement, whereas C3 showed the lowest initial stiffness due to lower initial prestressing and the amount of longitudinal reinforcement. It can be observed in the figure that the initial stiffness of the columns degraded at a higher rate up to 1% drift after which the rate of degradation reduced. Furthermore, it can be seen that the columns lost more than 50% of the initial stiffness up to a drift of 1%. Note that a sharp decrease in the initial stiffness of column C2 can be observed between 1% and 2% drift. This is mainly because after 1% drift column C2 was subjected to accidental load cycles of up to 4% drift. As a result, the column showed a sharp decrease in stiffness when subjected to the planned drift cycle of 2% after the accidental loading.

The comparison of the normalized stiffness of the tested columns with the conventional column from Raza et al. [51] in Fig. 18 shows that all the Fe-SMA prestressed columns exhibited a lower stiffness than the conventional column, despite a similar total axial load ratio. This is mainly due to the joint opening behavior in the Fe-SMA prestressed



columns, which increases the total column displacement due to the rocking component of the deformation, and thus reduces the column stiffness.

The effective stiffness of the columns was calculated from the force–displacement hysteresis based on the gradient of a line from the origin to the point where the column yields. The yield load of the column was determined from the force–displacement hysteresis using the reduced stiffness equivalent elastoplastic yield method [55]. In this method, the yield point is calculated based on the intersection of a line that passes from  $0.75 F_{max}$  and the horizontal line drawn from  $F_{max}$ . Table 5 presents the effective moment of inertia of the columns as a function of the gross moment of inertia. The effective moment of inertia was the highest for column C2 because a larger part of its cross-section was prestressed owing to the application of prestressing after the first layer of shotcrete as discussed previously. On the other hand, column C3 had the lowest effective moment of inertia owing to lower initial prestress.

The results in Table 5 show that the effective moment of inertia of Fe-SMA prestressed columns C1, C2, and C4 is lower than the conventional column, despite a similar axial load ratio. This is also mainly due to the increased flexibility of these columns due to the fixed-end rotation and rocking behavior.

### 3.9. Axial displacement-lateral drift behavior

The axial displacement of the column centerline was calculated by averaging the measurements of four SPOTs attached at the four corners of the loading block. The axial displacement of the columns with increasing lateral drifts is shown in Fig. 19. The columns experienced maximum axial elongation at maximum/minimum drifts and maximum shortening at the origin. The maximum elongation of the columns was found to be in the range of 3–4 mm at 5% drift and the maximum shortening was recorded as 0.4 mm at the origin. Column C2 showed a relatively higher elongation at the origin during accidental loading cycles as evident from Fig. 19 (b) mainly because its axial load was also fluctuating during the accidental load cycles.

It is interesting to note that no sharp increase in the shortening of the columns was observed up to drift levels of 5%. This implies that the columns were far from the limit state of collapse at the end of the experiment as typically the axial shortening of the columns drastically increases, as the column approaches the limit state of collapse.

## 4. Self-centering mechanism of columns reinforced with prestressed Fe-SMA bars

The self-centering ability of an RC column depends on the ratio of the self-centering moment to the resisting moment during the unloading of the column [5,56]. The self-centering moment results from the gravity load and prestressing forces acting on the column. The resisting moment, on the other hand, is created by the ED bars, which cause the column to lose its ability to re-center. A column can re-center effectively to its origin when the self-centering moment is greater than the resisting moment (i.e. self-centering index  $> 1$ ), as shown in Eq. (3). In Fe-SMA prestressed columns, the self-centering moment is the sum of the moment produced by the gravity load, and Fe-SMA bars until the complete loss of recovery stress in Fe-SMA bars. For small drift levels, the

self-centering moment can be expressed using Eq. (4) by taking the moment at the centroid of the concrete compression block (refer to Fig. 20). The resisting moment at small drift levels is only provided by ED bars and can be expressed by Eq. (5).

$$\text{self-centering index} = \frac{M_{sc}}{M_{resisting}} \quad (3)$$

Governing equations for moments before the loss of initial recovery stress:

$$M_{sc} = P_G \left( \frac{D}{2} - d_{FC} \right) + \sum_{i=1}^n F_{SMA,i} (d_{SMA,i} - d_{FC}) \quad (4)$$

$$M_{resisting} = \sum_{i=1}^n F_{ED,i} (d_{ED,i} - d_{FC}) \quad (5)$$

At large drift levels, the initial recovery stress of the Fe-SMA bars is completely lost, and the self-centering moment is provided by gravity loading alone, as expressed in Eq. (6). The Fe-SMA bars begin to contribute to the resisting moment after losing the initial prestress. Therefore, the resisting moment after the loss of the initial recovery stress is the sum of the moments due to the ED bars and the Fe-SMA bars, as expressed in Eq. (7).

Governing equations for moments after the loss of initial recovery stress:

$$M_{sc} = P_G \left( \frac{D}{2} - d_{FC} \right) \quad (6)$$

$$M_{resisting} = \sum_{i=1}^n F_{ED,i} (d_{ED,i} - d_{FC}) + \sum_{i=1}^n F_{SMA,i} (d_{SMA,i} - d_{FC}) \quad (7)$$

The self-centering and resisting moments were calculated for columns C1, C3, and C4 for target drift levels of 1% and 5%. To determine the self-centering index, the moments were calculated when the column was unloaded back to the origin from drifts of 1% and 5%. The initial recovery stress of Fe-SMA bars was assumed to be largely intact on unloading from 1% drift due to small strains in the bars and was considered to be completely lost at the 5% drift level owing to high strains in the bars. Accordingly, Eqs. (4) and (5) were used to determine the self-centering and resisting moments on unloading from 1% drift and Eqs. (6) and (7) were used to determine the corresponding moments on unloading from 5% drift. For the calculation of the moments, the Fe-SMA and steel bar forces were estimated based on the measurements of strains from the strain gauges. The equilibrium of moments about the centroid of the concrete compression block was used to determine the distance from the outermost fiber to the centroid of the concrete compression block ( $d_{FC}$ ), at 1% and 5% drift levels as expressed in Eq. (8). Fig. 20 shows the definition of various parameters required for the calculations.

$$M_{sc} + M_{resisting} = M_{ext} \quad (8)$$

The comparison of the self-centering ratio of columns C1, C3, and C4 on unloading from +1% and +5% drift is shown in Fig. 21. Note that the self-centering index was not calculated for drifts of 2%, 3%, and 4% because of the lack of information about the amount of remaining recovery stress in the bars at these drift levels. The results show that columns C1 and C3 have a quite high self-centering index of 97 and 57, respectively, on unloading from +1% drift. This is mainly because these columns were reinforced with only two ED bars that were located at the mid-section depth, thereby resulting in a small resisting moment while the self-centering moment was quite high owing to the initial prestress and gravity load. On the other hand, column C4 has a self-centering index of 22 because of relatively larger resisting moments due to 6 ED bars. Nonetheless, all three columns showed effective self-centering at +1% drift because the self-centering moment was quite higher than the resisting moment. In contrast, the self-centering moment of the columns

**Table 5**  
Effective moment of inertia of the columns.

Specimen	Effective Moment of Inertia $I_{eff}$
C1	$0.28 I_g$
C2	$0.30 I_g$
C3	$0.25 I_g$
C4	$0.28 I_g$
Conventional [51]	$0.36 I_g$

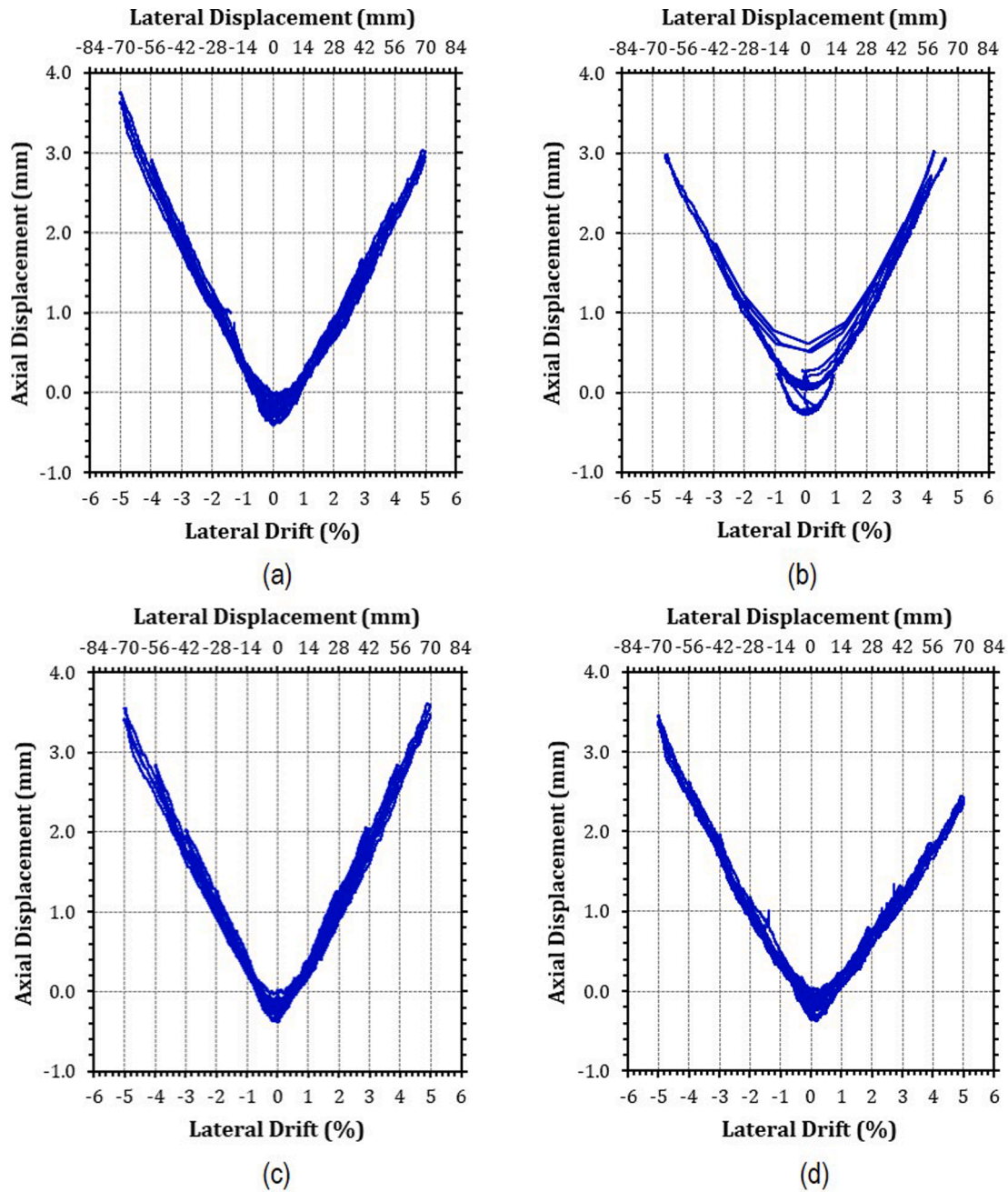


Fig. 19. Axial displacement-lateral drift behavior of the columns: a) C1; b) C2; c) C3; d) C4.

was quite less than the resisting moment on unloading from +5% drift, thereby resulting in a low self-centering index (i.e.  $<1$ ). This is because, at 5% drift, Fe-SMA bars completely lost their initial recovery stress and began contributing to the resisting moment. Accordingly, the self-centering index of columns C1, C3, and C4 on unloading from +5% drift were determined to be 0.13, 0.18, and 0.07, respectively. The residual drifts of the columns on unloading from +5% drift correlate well with the calculated self-centering index i.e.  $C3 < C1 < C4$ .

The results of this study indicate that the self-centering mechanism of the prestressed Fe-SMA bars differs from that of unbonded conventional tendons. Unlike conventional tendons that remain elastic and contribute minimally to energy dissipation, Fe-SMA bars lose their initial recovery stress at high drifts and begin to contribute to the energy dissipation of the column. From a design perspective, this suggests that a smaller amount of ED bars can be provided to meet the energy dissipation requirements of Fe-SMA prestressed columns compared to the columns

prestressed with conventional tendons. However, this also means that the reduction of residual drifts with Fe-SMA prestressing may be less than conventional prestressing. This aspect could be addressed in the future by developing Fe-SMA bars with higher yield strength and initial recovery stress using different thermo-mechanical treatments [57–58]. Nonetheless, the results of this study show the feasibility of the proposed technique in reducing residual drifts. For a more comprehensive evaluation, it is recommended that the seismic performance of the Fe-SMA prestressed columns should be assessed under multidirectional lateral loading protocols, as they can significantly impact the drift capacity of the columns [59–60].

## 5. Conclusions

This study aimed at developing a robust self-centering technique using prestressed Fe-SMA bars to reduce the residual deformations in the

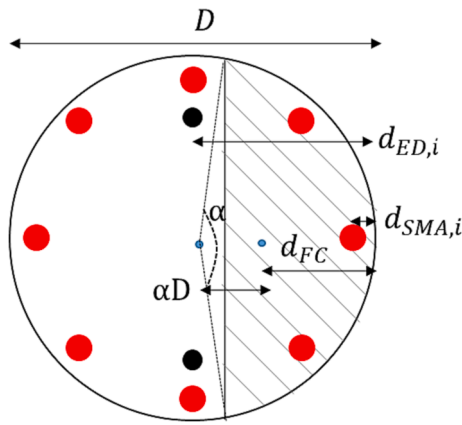


Fig. 20. Parameters defining the location of the concrete compression block.

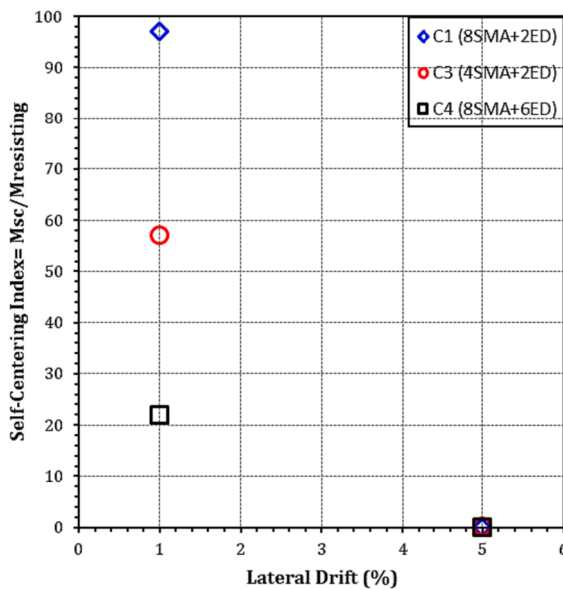


Fig. 21. Self-centering index of the columns on unloading from +1% and +5% drift levels.

existing concrete bridge columns under seismic loading. The efficacy of the proposed technique was studied by experiments on four large-scale specimens. The variable parameters of the study were the ratio of the amount of steel to SMA, the total amount of longitudinal reinforcement, and the initial prestress applied. The following conclusions can be drawn based on the results of this study:

1. The proposed technique successfully added self-centering capabilities to the columns and significantly reduced the residual drifts. The residual drifts of the columns were found to be 50–75% and 30–60% smaller than the conventional columns at target drifts of 3% and 5%, respectively. Furthermore, all the columns were able to sustain 5% drift without collapsing.
2. The proposed technique resulted in a controlled rocking mode of the column with a joint opening at the column-footing interface. The damage zone was more concentrated at the column-footing joint, resulting in less extensive damage compared to conventional columns.
3. The ratio of the amount of steel to prestressed Fe-SMA reinforcement ( $\frac{\rho_{steel}}{\rho_{sma}}$ ) significantly affected the residual drift of the columns. The columns with  $\frac{\rho_{steel}}{\rho_{sma}} = 0.15$  and 0.3 were able to maintain an average residual drift of  $\leq 1\%$  up to a target drift of 4%. With all other

parameters kept constant, a threefold increase in  $\frac{\rho_{steel}}{\rho_{sma}}$  from 0.15 to 0.45 approximately doubled the residual drift of the column for target drifts  $\geq 3\%$ .

4. The column with  $\frac{\rho_{steel}}{\rho_{sma}} = 0.45$  exhibited 32% higher energy dissipation compared to the column with  $\frac{\rho_{steel}}{\rho_{sma}} = 0.15$ . However, its residual drift at a target drift of 5% was also about 75% higher in comparison. Thus, among the alternatives considered in this study, the design with  $\frac{\rho_{steel}}{\rho_{sma}} = 0.15$  resulted in an adequate balance between energy dissipation and low residual drifts and is, therefore, the recommended design.
5. Fe-SMA prestressed columns exhibit a different self-centering and energy dissipation mechanism than conventional prestressed columns. In conventional columns, unbonded tendons remain elastic until column failure and contribute minimally to energy dissipation. In contrast, in this study, the outermost Fe-SMA bars in the column yielded and lost prestress at 2% drift and began to contribute to the energy dissipation thereafter. For drifts  $\geq 2\%$ , self-centering was achieved through the bars near the neutral axis, which partially retained prestress up to 5% drift. Thus, prestressed Fe-SMA bars can provide both self-centering and energy dissipation to the column, whereas conventional tendons only provide self-centering and require additional measures for energy dissipation.

The results of this study show that prestressed Fe-SMA bars can be a promising alternative to conventional post-tensioning techniques for adding a self-centering behavior into vertical structural members. Future studies may consider the application of prestressed Fe-SMA bars in the design of new structures, including precast segmental columns and walls with self-centering characteristics.

#### CRediT authorship contribution statement

**Saim Raza:** Conceptualization, Methodology, Investigation, Formal analysis, Writing – original draft. **Robert Widmann:** Methodology, Investigation, Formal analysis, Writing – review & editing. **Julien Michels:** Conceptualization, Methodology, Resources, Writing – review & editing. **M. Saiid Saiidi:** Conceptualization, Methodology, Writing – review & editing. **Masoud Motavalli:** Conceptualization, Methodology, Writing – review & editing. **Moslem Shahverdi:** Conceptualization, Methodology, Writing – review & editing, Supervision, Funding acquisition.

#### Declaration of Competing Interest

The authors declare that they have no known competing financial interests or personal relationships that could have appeared to influence the work reported in this paper.

#### Data availability

Data will be made available on request.

#### Acknowledgements

The financial support from the Swiss Innovation Agency (grant no. 39259.1 IP-ENG) and the technical assistance provided by the Structural Engineering Laboratory staff at Empa is gratefully acknowledged. The authors are also grateful to the industrial partner, re-fer AG, for providing the materials and technical support.

#### References

- [1] Phan V, Saiidi MS, Anderson J, Ghasemi H. Near-Fault Ground Motion Effects on Reinforced Concrete Bridge Columns. *J Struct Eng* 2007;133(7):982–9. [https://doi.org/10.1061/\(ASCE\)0733-9445\(2007\)133:7\(982\)](https://doi.org/10.1061/(ASCE)0733-9445(2007)133:7(982)).



- [2] Kawashima K, MacRae Gregory A, Hoshikuma J-I, Nagaya K. Residual displacement response spectrum. *J Struct Eng* 1998;124(5):523–30.
- [3] Jeong HI, Sakai J, Mahin SA. Shaking table tests and numerical investigation of self-centering reinforced concrete bridge columns. PEER Rep. 2008/06, Berkeley, CA: University of California; 2008.
- [4] Mohebbi A, Saiidi MS, Itani AM. Shake Table Studies and Analysis of a PT-UHPC Bridge Column with Pocket Connection. *J Struct Eng*. 2018;144(4):04018021. [http://doi.org/10.1061/\(ASCE\)ST.1943-541X.0001997](http://doi.org/10.1061/(ASCE)ST.1943-541X.0001997).
- [5] Cohagen LS, Pang JBK, Eberhard MO, Stanton JF. A precast concrete bridge bent designed to recenter after an earthquake. Rep. No. WA-RD 684.3, Washington State Transportation Center, Seattle; 2008.
- [6] Zhang Q, Alam MS. State-of-the-Art Review of Seismic-Resistant Precast Bridge Columns. *J Bridg Eng* 2020;25(10):03120001. [https://doi.org/10.1061/\(ASCE\)BE.1943-5592.0001620](https://doi.org/10.1061/(ASCE)BE.1943-5592.0001620).
- [7] Hewes JT, Priestley MN. Seismic design and performance of precast concrete segmental bridge columns. Rep. No. SSRP 2001/25. La Jolla, CA: Univ. of California San Diego; 2002.
- [8] Chou C-C, Chen Y-C. Cyclic tests of post-tensioned precast CFT segmental bridge columns with unbonded strands. *Earthq Eng Struct Dyn* 2006;35(2):159–75. <https://doi.org/10.1002/eqe.512>.
- [9] Ou Y-C, Chiewanichakorn M, Aref Amjad J, Lee George C. Seismic Performance of Segmental Precast Unbonded Posttensioned Concrete Bridge Columns. *J Struct Eng* 2007;133(11):1636–47. [https://doi.org/10.1061/\(ASCE\)0733-9445\(2007\)133:11\(1636\)](https://doi.org/10.1061/(ASCE)0733-9445(2007)133:11(1636)).
- [10] Wang J-C, Ou Y-C, Chang K-C, Lee GC. Large-scale seismic tests of tall concrete bridge columns with precast segmental construction. *Earthq Eng Struct Dyn* 2008;37(12):1449–65. <https://doi.org/10.1002/eqe.824>.
- [11] Ou Y-C, Wang P-H, Tsai M-S, Chang K-C, Lee George C. Large-Scale Experimental Study of Precast Segmental Unbonded Posttensioned Concrete Bridge Columns for Seismic Regions. *J Struct Eng* 2010;136(3):255–64. [https://doi.org/10.1061/\(ASCE\)ST.1943-541X.0000110](https://doi.org/10.1061/(ASCE)ST.1943-541X.0000110).
- [12] Motaref S, Saiidi MS, Sanders DH. Experimental Study of Precast Bridge Columns with Built-In Elastomer. *Transp Res Rec* 2010;2202(1):109–16. <https://doi.org/10.3141/2202-14>.
- [13] Li C, Hao H, Zhang X, Bi K. Experimental study of precast segmental columns with unbonded tendons under cyclic loading. *Adv Struct Eng* 2017;21(3):319–34. <https://doi.org/10.1177/1369433217717119>.
- [14] Wang Z, Wang J-Q, Tang Y-C, Liu T-X, Gao Y-F, Zhang J. Seismic behavior of precast segmental UHPC bridge columns with replaceable external cover plates and internal dissipaters. *Eng Struct* 2018;177:540–55. <https://doi.org/10.1016/j.engstruct.2018.10.012>.
- [15] Marriott D, Pampanin S, Palermo A. Quasi-static and pseudo-dynamic testing of unbonded post-tensioned rocking bridge piers with external replaceable dissipaters. *Earthq Eng Struct Dyn* 2009;38(3):331–54. <https://doi.org/10.1002/eqe.857>.
- [16] Bu Z-Y, Ou Y-C, Song J-W, Zhang N-S, Lee George C. Cyclic Loading Test of Unbonded and Bonded Posttensioned Precast Segmental Bridge Columns with Circular Section. *J Bridg Eng* 2016;21(2):04015043. [https://doi.org/10.1061/\(ASCE\)BE.1943-5592.0000807](https://doi.org/10.1061/(ASCE)BE.1943-5592.0000807).
- [17] Piras S, Palermo A, Saiidi MS. State-of-the-Art of Posttensioned Rocking Bridge Substructure Systems. *J Bridg Eng* 2022;27(3):03122001. [https://doi.org/10.1061/\(ASCE\)BE.1943-5592.0001833](https://doi.org/10.1061/(ASCE)BE.1943-5592.0001833).
- [18] Kurama Yahya C, Sritharan S, Fleischman Robert B, Restrepo Jose I, Henry Richard S, Cleland Ned M, et al. Seismic-Resistant Precast Concrete Structures: State of the Art. *J Struct Eng* 2018;144(4):03118001. [https://doi.org/10.1061/\(ASCE\)ST.1943-541X.0001972](https://doi.org/10.1061/(ASCE)ST.1943-541X.0001972).
- [19] Shahverdi M, Raza S, Ghafoori E, Czaderski C, Michels J, Motavalli M. Recent Advancements in Development and Application of an Iron-based Shape Memory Alloy at Empa. *Chimia* 2022;76(3):242. <https://doi.org/10.2533/chimia.2022.242>.
- [20] Michels J, Shahverdi M, Czaderski C, El-Hacha R. Mechanical Performance of Iron-Based Shape-Memory Alloy Ribbed Bars for Concrete Prestressing. *ACI Mater J* 2018;115(6). <https://doi.org/10.14359/51710959>.
- [21] Shahverdi M, Michels J, Czaderski C, Motavalli M. Iron-based shape memory alloy strips for strengthening RC members: Material behavior and characterization. *Constr Build Mater* 2018;173:586–99. <https://doi.org/10.1016/j.conbuildmat.2018.04.057>.
- [22] Raza S, Shafei B, Saiidi MS, Motavalli M, Shahverdi M. Shape memory alloy reinforcement for strengthening and self-centering of concrete structures—State of the art. *Constr Build Mater* 2022;324:126628. <https://doi.org/10.1016/j.conbuildmat.2022.126628>.
- [23] Michels J, Shahverdi M, Czaderski C. Flexural strengthening of structural concrete with iron-based shape memory alloy strips. *Struct Concr* 2018;19(3):876–91. <https://doi.org/10.1002/suco.201700120>.
- [24] Rojeb H, El-Hacha R. Self-Prestressing Using Iron-Based Shape Memory Alloy for Flexural Strengthening of Reinforced Concrete Beams. *ACI Struct J* 2017;114(2). <https://doi.org/10.14359/51689455>.
- [25] Hong K, Lee S, Yeon Y, Jung K. Flexural Response of Reinforced Concrete Beams Strengthened with Near-Surface-Mounted Fe-Based Shape-Memory Alloy Strips. *Int J Concr Struct Mater* 2018;12(1):45. <https://doi.org/10.1186/s40069-018-0279-y>.
- [26] Strieder E, Aigner C, Petautschnig G, Horn S, Marcon M, Schwenn M, et al. Strengthening of Reinforced Concrete Beams with Externally Mounted Sequentially Activated Iron-Based Shape Memory Alloys. *Materials* 2019;12(3). <https://doi.org/10.3390/ma12030345>.
- [27] Schranz B, Michels J, Czaderski C, Motavalli M, Vogel T, Shahverdi M. Strengthening and prestressing of bridge decks with ribbed iron-based shape memory alloy bars. *Eng Struct* 2021;241:112467. <https://doi.org/10.1016/j.engstruct.2021.112467>.
- [28] Schranz B, Wagner P-R, Czaderski C, Shahverdi M. Fibre optic measurements and model uncertainty quantification for Fe-SMA strengthened concrete structures. *Eng Struct* 2022;256:114005. <https://doi.org/10.1016/j.engstruct.2022.114005>.
- [29] Montoya-Coronado LA, Ruiz-Pinilla JG, Ribas C, Cladera A. Experimental study on shear strengthening of shear critical RC beams using iron-based shape memory alloy strips. *Eng Struct* 2019;200:109680. <https://doi.org/10.1016/j.engstruct.2019.109680>.
- [30] Cladera A, Montoya-Coronado LA, Ruiz-Pinilla JG, Ribas C. Shear strengthening of slender reinforced concrete T-shaped beams using iron-based shape memory alloy strips. *Eng Struct* 2020;221:111018. <https://doi.org/10.1016/j.engstruct.2020.111018>.
- [31] Czaderski C, Shahverdi M, Michels J. Iron based shape memory alloys as shear reinforcement for bridge girders. *Constr Build Mater* 2021;274:121793. <https://doi.org/10.1016/j.conbuildmat.2020.121793>.
- [32] Schranz B, Czaderski C, Vogel T, Shahverdi M. Bond behaviour of ribbed near-surface-mounted iron-based shape memory alloy bars with short bond lengths. *Mater Des* 2020;191:108647. <https://doi.org/10.1016/j.matdes.2020.108647>.
- [33] Schranz B, Czaderski C, Vogel T, Shahverdi M. Bond investigations of prestressed, near-surface-mounted, ribbed memory-steel bars with full bond length. *Mater Des* 2020;196:109145. <https://doi.org/10.1016/j.matdes.2020.109145>.
- [34] Fawaz G, Murcia-Delso J. Bond behavior of iron-based shape memory alloy reinforcing bars embedded in concrete. *Mater Struct* 2020;53(5):114. <https://doi.org/10.1617/s11527-020-01548-y>.
- [35] Abouali S, Shahverdi M, Ghassemieh M, Motavalli M. Nonlinear simulation of reinforced concrete beams retrofitted by near-surface mounted iron-based shape memory alloys. *Eng Struct* 2019;187:133–48. <https://doi.org/10.1016/j.engstruct.2019.02.060>.
- [36] Rezapour M, Ghassemieh M, Motavalli M, Shahverdi M. Numerical Modeling of Unreinforced Masonry Walls Strengthened with Fe-Based Shape Memory Alloy Strips. *Materials* 2021;14(11):2961. MDPI AG. <https://doi.org/10.3390/ma14112961>.
- [37] Dolatabadi N, Shahverdi M, Ghassemieh M, Motavalli M. RC Structures Strengthened by an Iron-Based Shape Memory Alloy Embedded in a Shotcrete Layer—Nonlinear Finite Element Modeling. *Materials* 2020;13(23). <https://doi.org/10.3390/ma13235504>.
- [38] Ghowsi AF, Sahoo DR, Kumar PCA. Cyclic tests on hybrid buckling-restrained braces with Fe-based SMA core elements. *J Constr Steel Res* 2020;175:106323. <https://doi.org/10.1016/j.jcsr.2020.106323>.
- [39] Ghowsi AF, Sahoo DR. Near-field earthquake performance of SC-BRBs with optimal design parameters of SMA. *J Constr Steel Res* 2020;175:106321. <https://doi.org/10.1016/j.jcsr.2020.106321>.
- [40] Ghowsi AF, Sahoo DR. Seismic response of SMA-based self-centering buckling-restrained frames under near-fault ground motions. *Soil Dyn Earthq Eng* 2020;139:106397. <https://doi.org/10.1016/j.soildyn.2020.106397>.
- [41] EN 1992-2. Eurocode 2: Design of concrete structures - Part 2: Concrete bridges - Design and detailing rules 2005.
- [42] EN 1998-2. Eurocode 8: Design of structures for earthquake resistance - Part 2: Bridges 2005.
- [43] Raza S, Michels J, Schranz B, Shahverdi M. Anchorage behavior of Fe-SMA rebars Post-Installed into concrete. *Eng Struct* 2022;272:114960. <https://doi.org/10.1016/j.engstruct.2022.114960>.
- [44] Sika Schweiz AG Technical Data Sheet SikaGrout-311 (2013).
- [45] Raza S, Michels J, Shahverdi M. Uniaxial behavior of pre-stressed iron-based shape memory alloy rebars under cyclic loading reversals. *Constr Build Mater* 2022;326:126900. <https://doi.org/10.1016/j.conbuildmat.2022.126900>.
- [46] Sika Schweiz AG Product Data Sheet Sika MonoTop®-412 N (2020).
- [47] Sika Schweiz AG Product Data Sheet Sika MonoTop®-910 N (2021).
- [48] EN, Eurocode 2: Design of concrete structures – Part 1–1: General rules and rules for buildings. Brussels: European Committee for Standardisation; 1992-1-1 (2004)..
- [49] Ichinose T. Splitting Bond Failure of Columns Under Seismic Action. *ACI Struct J* 1995;92(5). <https://doi.org/10.14359/904>.
- [50] Lura P, Plizzari GA, Riva P. 3D finite-element modelling of splitting crack propagation. *Mag Concr Res* 2002;54(6):481–93. <https://doi.org/10.1680/macrcr.2002.54.6.481>.
- [51] Raza S, Menegon SJ, Tsang H-H, Wilson JL. Collapse Performance of Limited Ductile High-Strength RC Columns under Unidirectional Cyclic Actions. *J Struct Eng*. 2020;146(10):04020201. [http://doi.org/10.1061/\(ASCE\)ST.1943-541X.0002772](http://doi.org/10.1061/(ASCE)ST.1943-541X.0002772).
- [52] Liu X, Li J, Tsang H-H, Wang J, Zhong J. Experimental evaluation of seismic performance of unbonded prestressed reinforced concrete column. *Eng Struct* 2020;208:109913. <https://doi.org/10.1016/j.engstruct.2019.109913>.
- [53] Lee WK, Billington SL. Performance-based earthquake engineering assessment of a self-centering, post-tensioned concrete bridge system. *Earthq Eng Struct Dyn* 2011;40(8):887–902. <https://doi.org/10.1002/eqe.1065>.
- [54] Japan Road Association. Design specifications of highway bridges. Tokyo, Japan: Part V seismic design. Maruzen; 2002.
- [55] Park R. Ductility Evaluation from Laboratory and Analytical Testing-State of the Art; 1988.
- [56] Hieber D, Wacker J, Eberhard M, Stanton John F. Precast Concrete Pier Systems for Rapid Construction of Bridges in Seismic Regions. Washington State Department of Transportation Report No. WA-RD-611.1, Washington State Department of Transportation, Washington, 2005.
- [57] Yang Y, Leinenbach C, Shahverdi M. Simulation and experimental characterization of VC precipitation and recovery stress formation in an FeMnSi-based shape

- memory alloy. *J Alloy Compd* 2023;940:168856. <https://doi.org/10.1016/j.jallcom.2023.168856>.
- [58] Yang Y, Arabi-Hashemi A, Leinenbach C, Shahverdi M. Influence of thermal treatment conditions on recovery stress formation in an FeMnSi-SMA. *Mater Sci Eng A* 2021;802:140694. <https://doi.org/10.1016/j.msea.2020.140694>.
- [59] Raza S, Menegon SJ, Tsang H-H, Wilson JL. Axial Load Variation of Columns in Symmetrical RC Buildings Subject to Bidirectional Lateral Actions in Regions of Low to Moderate Seismicity. *J Earthq Eng* 2022;26(5):2701–29. <https://doi.org/10.1080/13632469.2020.1772151>.
- [60] Raza S, Tsang H-H, Menegon Scott J, Wilson John L. Generalized Loading Protocols for Experimentally Simulating Multidirectional Earthquake Actions on Building Columns in Regions of Low-to-Moderate Seismicity. *J Struct Eng* 2021;147(7):04021082. [https://doi.org/10.1061/\(ASCE\)ST.1943-541X.0003056](https://doi.org/10.1061/(ASCE)ST.1943-541X.0003056).